

Mechanistic model of an in-line liquid-liquid swirl separator

G. J. de Zoeten

Mechanistic model of an in-line liquid-liquid swirl separator

by

G. J. de Zoeten

in partial fulfillment of the requirements for the degree of

Bachelor of Science
in Applied Physics

at the Delft University of Technology,
to be defended publicly on Thursday July 19, 2018 at 10:00 AM.

Thesis committee: L. Portela Supervisor
C.R. Kleijn TU Delft

An electronic version of this thesis is available at <http://repository.tudelft.nl/>.

ABSTRACT

The world's ever-increasing demand for energy and the inevitable depletion of the available fossil resources in the foreseeable future lead to an increasing necessity to optimize the exploitation of oil fields. The in-line liquid-liquid swirl separator is a separation method that is interesting for two reasons: It separates oil and water faster than the conventional settling tank and the fact that it is placed in-line is a practical advantage. In this report a study has been conducted on the modelling of an in-line liquid-liquid swirl separator using a mechanistic model. This model can be used as a thinking tool to better understand the separation performance of an in-line swirl separator: which parameters play an important role, what are the key processes? This model could also serve as an engineering design tool to optimize the swirl separator for industrial use. The goal of this research is to build a solid foundation for a relatively uncomplicated mechanistic model to describe the underlying physical processes of an in-line swirl separator.

To model the process of separating an oil-water mixture using an in-line liquid-liquid swirl separator different research steps have been taken. The first step was building a base model. The idea of this model was to provide a solid foundation for a more sophisticated model. Based on the findings from this base model and by comparing the base model results to results from CFD simulations and experimental results, a more sophisticated model has been built. In this report this model is referred to as the swirl decay model. These models calculate the separation efficiency based on certain key parameters. To find the efficiency, the trajectory of the particle in the axial and radial directions are modelled based on a balance of forces constructed under the assumption of a quasi-steady state. From these trajectories it is possible to determine whether an oil droplet starting at a certain radial position at the beginning of the swirl tube ends up in the collection tube at the end of the pipe.

The mechanistic model that was built in this research manages to capture the general processes involved in an in-line swirl separator, although the calculated efficiency values are generally larger than the experimental values. However, in order to capture the whole process, several features should be added to the model. These improvements include: more accurately determining the swirl decay coefficient, finding a way to model the droplet size distribution, model droplet coalescence and breakup, implementing a way to alter the flow split.

CONTENTS

Abstract	i
List of Figures	iv
1 Introduction	1
1.1 Background motivation	1
1.2 In-line swirl separator	1
1.3 Research	2
1.4 Thesis outline	3
2 Fundamental Theoretical background	4
2.1 Fluid Equations of Motion	4
2.2 Swirling flow	4
2.2.1 Swirl decay	5
2.2.2 Vorticity and circulation	6
2.2.3 Vortex breakdown	6
2.3 Vortex solutions	7
2.3.1 Rankine Vortex	7
2.3.2 Gaussian vortex	8
2.4 Flow split	8
2.5 Forces on the oil droplet	9
2.5.1 Trajectory forces	9
2.5.2 Particle breakup	9
2.5.3 Particle coalescence	10
2.6 Separation performance	10
3 Base model for an in-line swirl separator	11
3.1 Assumptions	11
3.2 Model outline	11
3.3 Balance of forces	13
3.3.1 Separation efficiency	14
3.4 Non-Dimensional analysis	14
3.4.1 Non-dimensional numbers	14
3.5 Non-dimensional results	16
3.5.1 Buoyancy force vs. Inertial forces	17
3.5.2 Radial Reynolds number	17
3.5.3 Consistency of Non-Dimensional results	18
3.6 Parameter influence	18
3.6.1 Vorticity	18
3.6.2 Particle diameter	19
3.7 Conclusions	20
4 Base model comparison with CFD and experiments	21
4.1 Comparison with CFD	21
4.2 Comparison with experimental results	24
4.3 Conclusions	25

5	Swirl decay model	26
5.1	Assumptions	26
5.2	Model outline	26
5.3	Parameter influence	27
5.3.1	Strong swirling	28
5.3.2	Weak swirling	29
5.4	Conclusions.	31
6	Swirl decay model comparison with CFD and experiments	32
6.1	Comparison to CFD.	32
6.1.1	Efficiency comparison	33
6.2	Comparison with experiments	34
6.3	Conclusions.	37
7	Conclusions and recommendations	38
7.1	Conclusion	38
7.2	Recommendations	39
A	Additional base model results	40
A.1	Non-dimensional results	40
A.2	Parameter results	42
B	Additional swirl decay model results	44
B.1	Parameter results for strong swirling	44
C	Experimental droplet size distribution approximation	45
	Bibliography	47

LIST OF FIGURES

1.1	Schematic of an in-line liquid-liquid swirl separator	1
1.2	Schematic size comparison between an in-line swirl separator and a settling tank	2
2.1	Schematic overview of an in-line liquid-liquid swirl separator	5
2.2	The swirl decay coefficient as a function of the Reynolds number of the flow. The swirl decay coefficient tends to decrease as the Reynolds number of the flow increases	6
2.3	Schematic illustration of vortex breakdown and recirculation near the pick up tube in a swirl separator.	6
2.4	The azimuthal velocity and pressure distributions of a Rankine vortex as a function of the radial position	7
2.5	The azimuthal velocity and pressure distributions of a Gaussian vortex as a function of the radial position	8
3.1	Schematic of the in-line swirl separator with the geometry key parameters for the base mechanistic model	12
3.2	Schematic of the radial trajectory of a particle in an in-line swirl separator	12
3.3	The influence of the non-dimensional number $\frac{F_B}{F_I}$ on the separation efficiency.	17
3.4	The influence of the non-dimensional number Re_r on the separation efficiency.	17
3.5	The influence of ω on the separation performance of the base model.	19
3.6	The influence of particle diameter D_p on the separation performance of the base model.	19
4.1	Rankine vortex azimuthal velocity profile fitted to simulated velocity profile at $z = 0.50\text{m}$ by Slot.	22
4.2	Rankine vortex azimuthal velocity profile fitted to simulated velocity profile at $z = 1.50\text{m}$ by Slot.	22
4.3	The decay of circulation as a function of z for strong swirling.	23
4.4	Comparison between efficiencies calculated using CFD simulations [1], experimental results from van Campen [2] and the base model for strong swirling at different FS values.	24
5.1	The influence of the particle diameter D_p on the separation efficiency for the swirl decay model for strong swirling.	28
5.2	The influence of the swirl decay coefficient C_{dc} on the separation efficiency for the swirl decay model for strong swirling.	28
5.3	The influence of the ratio between the tube length L and the axial velocity U_z on the separation efficiency for the swirl decay model for strong swirling.	29
5.4	The influence of the particle diameter D_p on the separation efficiency for the swirl decay model for weak swirling.	29
5.5	The influence of the swirl decay coefficient C_{dc} on the separation efficiency for the swirl decay model for weak swirling.	30
5.6	The influence of the ratio between the tube length L and the axial velocity U_z on the separation efficiency for the swirl decay model for weak swirling.	30
6.1	Gaussian vortex azimuthal velocity profile fitted to simulated velocity profile at $z = 1.50\text{m}$ by Slot.	32
6.2	Comparison between efficiencies calculated using CFD by Slot and the swirl decay model for different particle diameters D_p and strong swirling. The oil inlet concentration is $\alpha = 0.25$	34
6.3	PDF of the number of droplets upstream and downstream of the strong and weak swirl element as a function of the droplet size. This distribution is determined experimentally by van Campen. Figure from van Campen [2].	35
6.4	Comparison between the dilute efficiency calculated by van Campen, Slot and the swirl decay model for different oil inlet concentrations c_{in} and different values for the flow split. Calculations for strong swirling.	36

6.5	The dilute efficiency experimentally determined by van Campen for weak and strong swirl, different FS values and $c_{in} = 0.25$	37
A.1	The influence of changing non-dimensional numbers on the separation efficiency while keeping other non-dimensional numbers constant. The influence of the parameters is displayed as follows. Top left: $\frac{D_o}{L}$, Top right: $\frac{D_p}{D_o}$, Bottom left: $\frac{\Omega R_v}{U_z}$, Bottom right: $\frac{D_v}{D_o}$. As can be seen from the figure, none of these non-dimensional numbers influences the efficiency when the other non-dimensional numbers are kept constant.	40
A.2	The influence of $\left(\frac{D_i}{D_o}\right)^2$ on the separation efficiency η	41
A.3	The influence of D_i/D_o on the separation performance of the base model.	42
A.4	The influence of changing parameters on the separation efficiency while keeping other parameters constant. The influence of the parameters is displayed as follows. Top left: $\frac{L}{U_z}$, Top right: $\frac{\Delta\rho}{\rho_f}$, Bottom left: $\frac{D_v}{D_o}$, Bottom right: μ_f	43
B.1	The influence of changing key parameters individually on the separation efficiency η while keeping other key parameters constant. The influence of the parameters is displayed as follows. Top left: $\left(\frac{D_i}{D_o}\right)^2$, Top right: μ_f , Bottom left: ω , Bottom right: $\frac{\Delta\rho}{\rho_f}$. The results are for strong swirling.	44
C.1	The bar chart approximating the particle size distributions of weak and strong swirling. Experimental results by van Campen [2].	45

1

INTRODUCTION

1.1. BACKGROUND MOTIVATION

The world's ever-increasing demand for energy and the inevitable depletion of the available fossil resources in the foreseeable future lead to an increasing necessity to optimize the exploitation of oil fields. Even though renewable energy sources supplying a vastly increasing fraction of the world's energy demand, the demand for oil is still high. Nowadays much of the oil-drilling sites are located offshore in deep water with depths exceeding 1000m.[3] At these sites, water is present in the soil. Due to the density difference between water and oil, with oil having the lower density, the oil floats on top of the water. During drilling, the oil will come up first, but after some time water will flow into the well-bore due to the difference in viscosity between water and oil.[2] As a result, an oil-water emulsion is extracted, which needs to be separated in order to obtain the desired oil. The conventional method to achieve this is the usage of settling tanks. However, settling tanks bear some disadvantages with them. First of all, the separation is based on the density difference between water and oil. The driving force behind the process is the gravitational force, which is not particularly strong. As a result this process takes a relatively long time. Secondly, large vessels are required to have sufficient separating capacity. At an off-shore location this is unpractical, as offshore platforms have a limited capacity to store such vessels. Since it is not economically viable to pump the oil-water mixture ashore before separating it, a solution is required to separate the oil-water mixture closer to the oil well.[4]

1.2. IN-LINE SWIRL SEPARATOR

An alternative method to separate oil and water that is based on the density difference as well, is an in-line swirl separator. This method uses a swirling element to force the fluid to rotate in order to generate centrifugal forces. Due to the density difference between the two phases, the magnitude of the centrifugal forces acting upon these phases differs, which results in separation. A collection tube is placed at the end of the pipe to collect the separated phases. The swirl separator is schematically illustrated in figure 1.1.

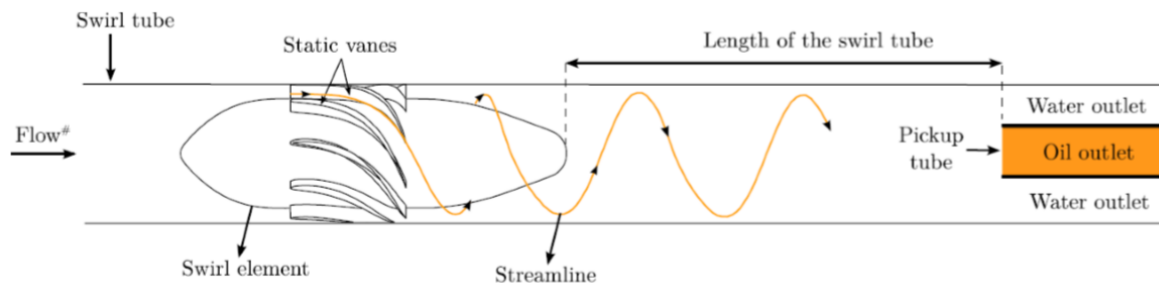


Figure 1.1: Schematic overview of the in-line swirl separator. The swirl separator consists of a swirling element, swirl tube and a pickup tube. Figure from A. Ashok [5].

The centrifugal acceleration can be much larger than the gravitational acceleration. Therefore, this method allows for faster phase separation than the conventional settling tanks. Another advantage of this method is that the swirl separator is mounted inside the pipe and is therefore in-line with the fluid. Therefore, it is not necessary to have storage tanks on the offshore platforms and the separated oil can be transported ashore directly. In figure 1.2 a size comparison between an in-line swirl separator and a settling tank is shown. From the figure it becomes clear that the swirl separator is smaller than the settling tank, which is an advantage for practical reasons as mentioned above.

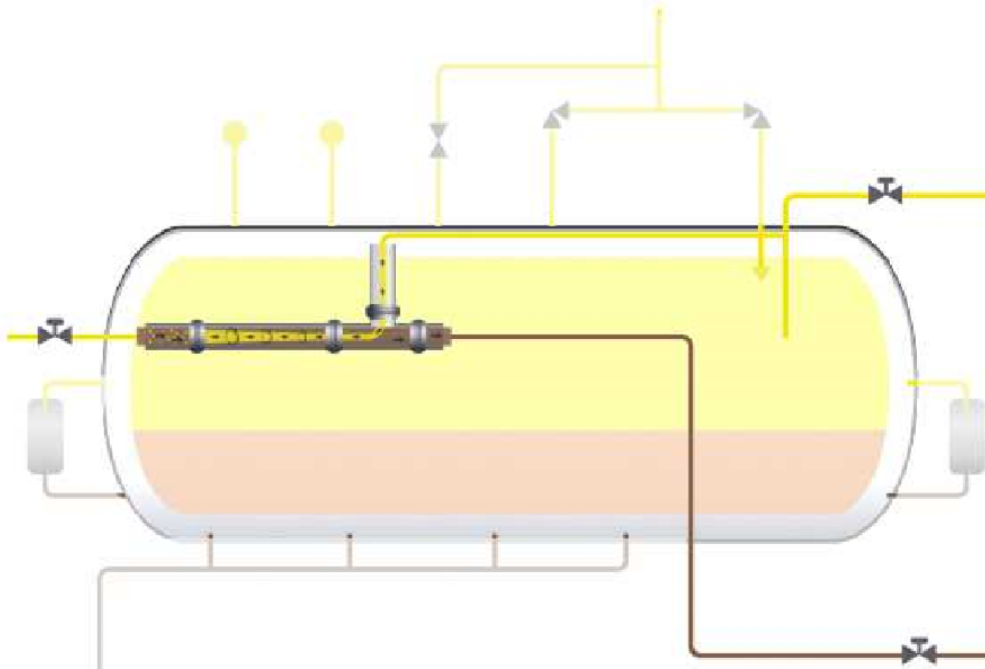


Figure 1.2: Schematic size comparison between an in-line swirl separator and a conventional settling tank. The in-line swirl separator is shown in the top left corner of the settling tank. The settling tank is clearly larger than the in-line swirl separator. Figure from Kristiansen [3].

1.3. RESEARCH

On this particular device, several researches have been conducted. Van Campen [2] built an experimental setup and performed measurements of single and multi-phase flow. Star [6] performed further measurements to single phase flow and researched the pressure distribution in the pipe. Slot [1] performed many computational fluid dynamics (CFD) simulations. The goal of this research is to build a solid foundation for a relatively uncomplicated mechanistic model to describe the underlying physical processes of an in-line swirl separator. This model can be used as a thinking tool to better understand the separation performance of an in-line swirl separator: which parameters play an important role, what are the key processes? This model could also serve as an engineering design tool to optimize the swirl separator for industrial use. The advantage of an uncomplicated model is that the required calculations to evaluate the situation could be executed instantaneously. Therefore, a future purpose for this model would be to control the separation performance of an in-line swirl separator in real time. This could be done when the influence of the key parameters on the separation performance is well understood. This research strives to take the first steps in designing such a model. The central research question dealt with in this report is:

To what extent can a mechanistic model predict the separation performance of an in an in-line liquid-liquid swirl separator?

1.4. THESIS OUTLINE

This thesis consists of seven chapters. Chapter 1 describes the background motivation for the project, the specific goals and how these goals are attempted to be achieved. The second chapter serves as theoretical background to support the understanding of the relevant physical processes. This chapter also addresses which physical processes will be addressed in this research. Chapter 3 describes the base model used in this research to describe the physical processes in an in-line swirl separator. This chapter also discusses which conclusions can be drawn based on this model and which aspects of the model require additional attention. Chapter 4 compares the results from the base model described in chapter 3 with results from previous experiments and CFD simulations. Chapter 5 describes how the base model from chapter 3 is improved to obtain a more sophisticated model. Chapter 6 compares this more sophisticated model to results from previous experiments and CFD simulations again. In chapter 7 conclusions are drawn and recommendations for further research are made.

2

FUNDAMENTAL THEORETICAL BACKGROUND

This chapter describes the relevant physical processes occurring in an in-line swirl separator. The fundamental components of the process are addressed.

2.1. FLUID EQUATIONS OF MOTION

This section discusses the equations of motion that are used to describe swirling motion. For these equations a cylindrical coordinate-system is chosen, since the system consists of a pipe section as schematically illustrated in figure 1.1. The coordinates in the radial, azimuthal and axial directions are represented by r , θ and z respectively. The corresponding velocity components are u_r , u_θ and u_z . Fluid motion can be described as conservation of mass and momentum, which are described by the continuity equation and the Navier-Stokes equations respectively. The viscosity of the continuous phase fluid is constant and the flow is incompressible, which means the fluid motion can be described by the incompressible momentum Navier-Stokes equation [6]:

$$\rho \left(\frac{\partial \vec{u}}{\partial t} + \vec{u} \cdot \nabla \vec{u} \right) = -\nabla p + \mu \nabla^2 \vec{u} + \vec{f} \quad (2.1)$$

In this equation ρ is the density of the fluid, μ is the viscosity of the fluid, p the pressure and \vec{f} the body forces. The mass conservation equation is given by:

$$\nabla \cdot \vec{u} = 0 \quad (2.2)$$

For the chosen cylindrical coordinate system this equation becomes

$$\frac{1}{r} \frac{\partial r u_r}{\partial r} + \frac{1}{r} \frac{\partial u_\theta}{\partial \theta} + \frac{\partial u_z}{\partial z} = 0 \quad (2.3)$$

These equations give a general idea of which quantities are conserved. For this research it is not relevant to study these equations in greater detail.

2.2. SWIRLING FLOW

Figure 2.1 gives a schematic overview of an in-line swirl separator. An in-line swirl separator contains a swirling element at the beginning of the swirl tube. This swirling element forces the liquid to swirl. In this section general theory about swirling flow is discussed. The intensity of swirl flow is often expressed in terms of the swirl number Ω , which gives the flux of angular momentum made dimensionless by the density, swirl tube radius and bulk velocity of the fluid [7]. In this thesis the swirl number will be used as defined by van Campen [2], Slot [1] and Knöbel [8].

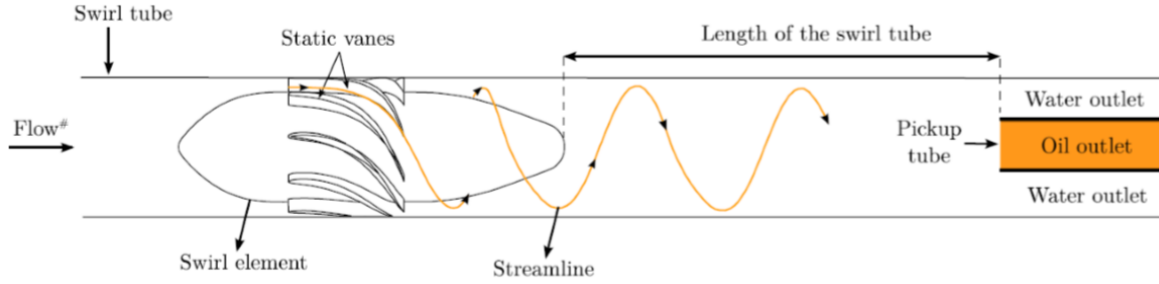


Figure 2.1: Schematic overview of the in-line swirl separator. The swirl separator consists of a swirling element, swirl tube and a pickup tube. Figure from A. Ashok [5].

$$\Omega(z) = \frac{\int_0^R \int_0^{2\pi} \rho_c u_\theta r u_z r d\theta dr}{\rho_c \pi R^3 u_b^2} \quad (2.4)$$

In equation 2.4 ρ_c is the density of the continuous phase, R is the radius of the swirl tube, u_θ is the azimuthal velocity component, u_z is the axial velocity component, r is the radial distance from the center of the swirl tube and u_b is the bulk velocity of the fluid. The swirl number Ω is given as a function of z , the downstream component. The integral in the numerator of equation 2.4 consists of two parts: the angular momentum of a finite volume ($\vec{r} \times \vec{p} = \rho_c r u_\theta dV$) and the distribution of the mass flux over the radius ($r u_z$). The denominator consists of two parts as well: The mass flux ($\rho_c \pi R^2 u_b$) and the $R u_b$ term. Because of this combination the swirl number is non-dimensional [2].

2.2.1. SWIRL DECAY

Directly downstream of the swirl element the swirl intensity will be at its maximum. However, the swirl is not constant over the entire length of the swirl tube. Due to wall friction in the swirl tube, the swirl intensity will decay when the continuous phase flows downstream. Experimental studies have revealed that this decay is exponential and can be described as in equation 2.5 [8]

$$\Omega(z) = \Omega_0 e^{(-C_{dc} \frac{z-z_0}{D})} \quad (2.5)$$

In this equation Ω_0 is the swirl number at the reference point, z_0 is the downstream coordinate of the reference point, D is the diameter of the swirl tube and C_{dc} is the swirl decay coefficient. The reference point is chosen at a point just downstream of the swirling element, where the swirling intensity is at its maximum. The swirl decay coefficient does not have a constant value, but is dependent on a number of parameters, such as the roughness of the pipe wall, the swirl intensity and the Reynolds number of the flow, which is defined in equation 2.6.

$$\text{Re}_D = \frac{\rho_c D_o u_b}{\mu_c} \quad (2.6)$$

In this equation ρ_c and μ_c are the density and dynamic viscosity of the continuous phase respectively. D_o is the diameter of the swirl tube and u_b is the bulk velocity of the flow. Figure 2.2 shows the swirl decay coefficient as a function of the Reynolds number of the flow for different experimental setups. From the figure it seems that generally the swirl decay coefficient tends to decrease for an increasing Reynolds number of the flow as defined in equation 2.6. Typical swirl decay coefficient values seem to be in the range of $0.01 < C_{dc} < 0.07$. The drawn line in figure 2.2 is the friction factor for fully developed pipe flow λ . The swirl decay coefficient C_{dc} seems to follow roughly the same trend as λ for increasing Reynolds number of the flow [9]. Also, the swirl decay coefficient seems to increase for larger swirl numbers [7].

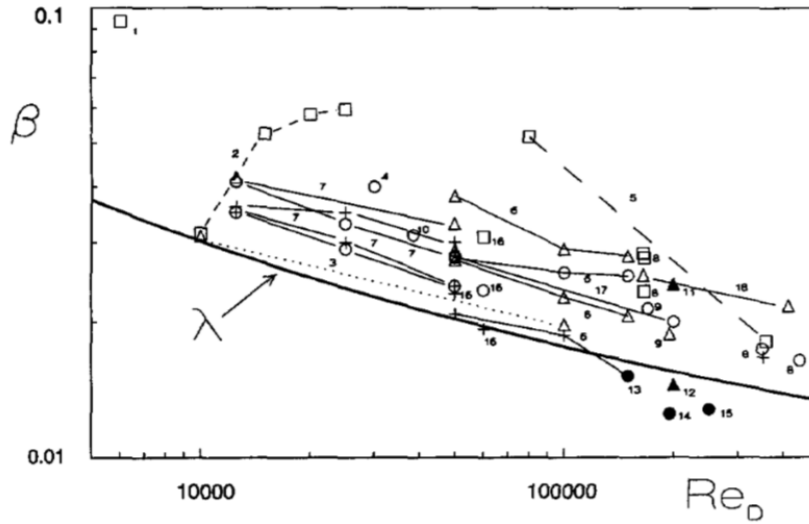


Figure 2.2: The swirl decay coefficient as a function of the Reynolds number of the flow. The decay coefficient C_{dc} is denoted as β on the vertical axis. Different symbols are experimental values of β for different experimental setups. λ is the friction factor for fully developed pipe flow. Figure copied from Dirkzwager [7].

2.2.2. VORTICITY AND CIRCULATION

Vorticity and circulation characterize the swirling flow. In this research the circulation is a key parameter, which is based on the vorticity. The vorticity is a vector field which can be derived from the velocity field. The vorticity is defined as [6]

$$\vec{\omega} = \nabla \times \vec{u} \quad (2.7)$$

From the vorticity $\vec{\omega}$ the circulation, which is a macroscopic measure of the rotation, can be calculated using equation 2.8:

$$\Gamma = \oint_C \vec{u} \cdot d\vec{l} = \iint_S (\nabla \times \vec{u}) \cdot d\vec{A} = \iint_S \vec{\omega} \cdot d\vec{A} \quad (2.8)$$

The circulation is calculated by taking the closed contour integral of the velocity field, which can be converted into a surface integral using Stokes theorem. The circulation is a measure of the strength of the vortex.

2.2.3. VORTEX BREAKDOWN

At large enough swirl numbers swirling flow exhibits a region at the vortex axis where reverse axial flow occurs. This phenomenon, called vortex breakdown, is not observed at low swirl numbers. This reverse flow is characterised by the formation of an internal stagnation point on the vortex axis. The radius of the vortex decays downstream and has become small at the stagnation point. Downstream of this stagnation point, a limited reverse flow region is established. These phenomena are schematically illustrated in figure 2.3. Several theories about vortex breakdown exist, but the most predominant theory, especially for large swirl numbers, is the bubble like breakdown. In this case a bubble-shaped recirculation zone appears behind the stagnation point. After this recirculation zone the axial velocity becomes positive again. [7] This recirculation may have effects on the oil-water separation performance of the system.

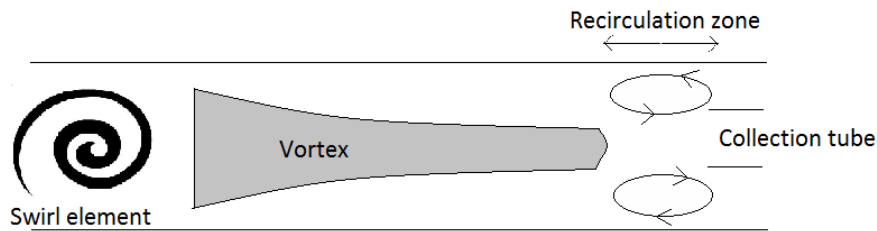


Figure 2.3: Schematic illustration of vortex breakdown and recirculation near the pick up tube in a swirl separator.

2.3. VORTEX SOLUTIONS

The swirling flow in the pipe can assume different forms. In this section two vortex types that are commonly used are described.

2.3.1. RANKINE VORTEX

The Rankine vortex consists of a forced vortex in the inner zone and a free vortex in the outer zone. This type of vortex does not have a velocity component in the radial direction, but only has an azimuthal velocity component. The angular velocity is given by the following expression:

$$\Omega = \frac{\Gamma}{2\pi R_c^2} \quad (2.9)$$

In equation 2.9 Γ is the circulation as calculated in equation 2.8. R_c is the radius of the vortex core, the inner zone. The azimuthal velocity u_θ for the inner and outer zone of the vortex are described as follows [6]

$$u_\theta(r) = \begin{cases} \Omega r & \text{if } r < R_c \\ \frac{\Omega R_c^2}{r} & \text{if } r \geq R_c \end{cases} \quad (2.10)$$

From this and equations 2.1 and 2.3 the following pressure distributions can be calculated [8]

$$p(r) - p_0 = \begin{cases} -\rho\Omega^2 R_c^2 + \frac{1}{2}\rho\Omega^2 r^2 & \text{if } r < R_c \\ -\frac{1}{2}\frac{\rho\Omega^2 R_c^4}{r^2} & \text{if } r \geq R_c \end{cases} \quad (2.11)$$

In these equations ρ is the density of the continuous phase. The azimuthal velocity u_θ and the pressure p as a function of the radial position r are illustrated in figure 2.4.

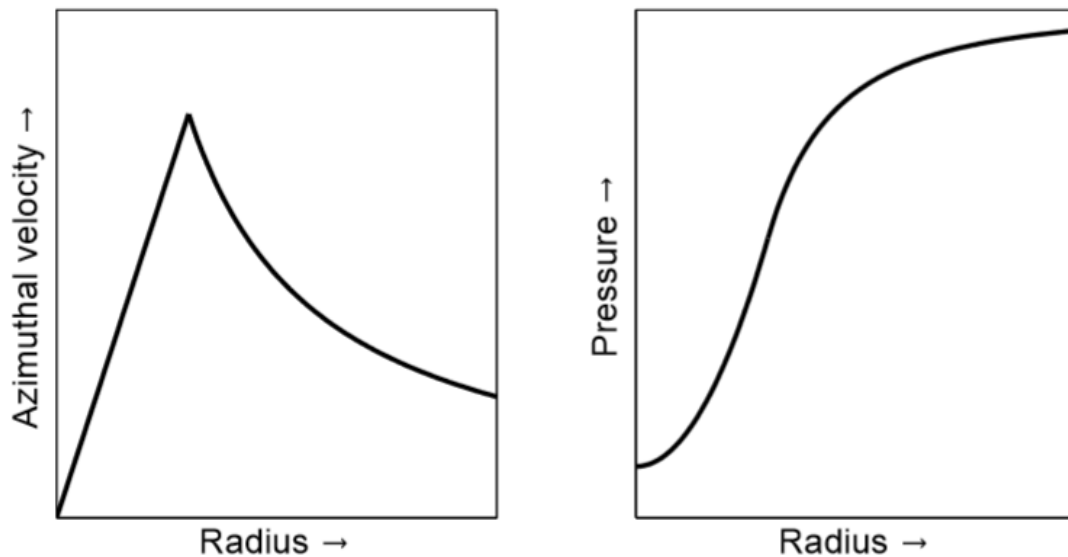


Figure 2.4: Azimuthal velocity distribution and corresponding pressure distribution of a Rankine vortex. Figure copied from Star [6].

2.3.2. GAUSSIAN VORTEX

Like the Rankine vortex, the Gaussian vortex does not have a radial velocity component. However, as opposed to the Rankine vortex, the azimuthal velocity profile of a Gaussian vortex does not consist of an inner and outer zone. The azimuthal velocity is calculated as follows

$$u_{\theta}(r) = \frac{\Gamma}{2\pi r} \left(1 - e^{-\frac{\gamma r^2}{R_c^2}} \right) \quad (2.12)$$

In this equation, Γ is the circulation, and u_{θ} reaches its maximum at the core radius R_c . The constant γ has the value $\gamma = 1.256431$. The pressure distribution corresponding to this velocity distribution is given as

$$p(r) = -\frac{1}{2} \rho u_{\theta}^2 - \frac{\gamma \rho \Gamma^2}{4\pi R_c^2} \left(E_1 \left(\frac{\gamma r^2}{R_c^2} \right) - E_1 \left(\frac{\gamma^2 r^2}{R_c^2} \right) \right) \quad (2.13)$$

In this expression E_1 is the standard exponential integral, which is defined as

$$E_1 = \int_x^{\infty} \frac{e^{-t}}{t} dt \quad (2.14)$$

The azimuthal velocity u_{θ} and the pressure p as a function of the radial position r are illustrated in figure 2.5.

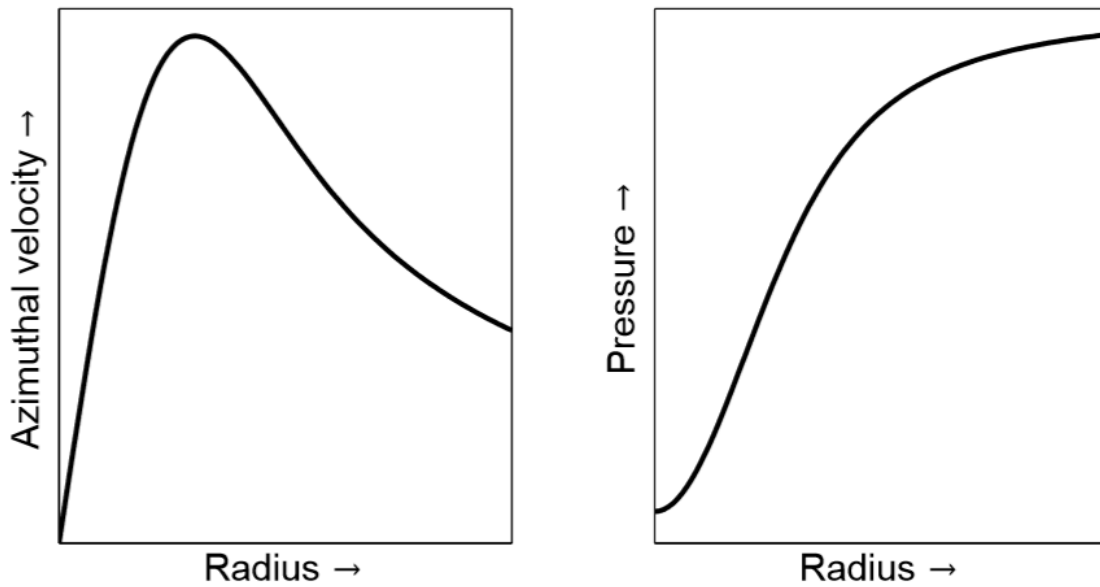


Figure 2.5: Azimuthal velocity distribution and corresponding pressure distribution of a Gaussian vortex. Figure copied from Star [6].

2.4. FLOW SPLIT

The flow split (FS) is another parameter that affects the separation performance of the in-line swirl separator. At the end of the swirl tube a tube with smaller diameter is placed in the center of the tube. This is the pickup tube. A schematic of the in-line swirl separator is shown in figure 2.1. The 'oil outlet' in figure 2.1 is called the Light Phase Outlet LPO. The 'water outlet' is called the Heavy Phase Outlet (HPO). When the flow arrives at the end of the swirl tube, part of the flow will end up in the LPO and part of the flow will end up in the HPO. Knöbel defined the flow split as the fraction of the total volumetric flow that ends up in the LPO.[8]

$$FS = \frac{\phi_{LPO}}{\phi_{LPO} + \phi_{HPO}} \quad (2.15)$$

The FS can be controlled using two valves at the end of the swirling tube, controlling the volumetric flow in the HPO and LPO. Recirculation effects near the collection tube as schematically shown in figure 2.3 also affect the FS but will not be considered in this study.

2.5. FORCES ON THE OIL DROPLET

Due to interaction between the continuous phase and the dispersed oil droplet, several forces are acting upon the oil droplet. These forces arise from velocity and, viscosity and density differences between the continuous phase and the oil droplet. These forces play a key role in the separation performance of the system. In this study the following forces will be considered.

- Drag force
- Buoyancy force
- Surface tension force

2.5.1. TRAJECTORY FORCES

The trajectory of the particle primarily depends on two forces:

- Drag force
- Buoyancy force

The radial velocity of the oil droplet u_r depends on these two forces as explained in more detail in section 3.2. The radial velocity is linked directly to the separation performance of the system, as the radial velocity determines at which radial position the oil droplet is going to end up: either inside the pickup tube or not. The drag force [8] is expressed as

$$F_D = \frac{1}{2} \rho_c C_D A_d |\langle \mathbf{u}_d \rangle - \langle \mathbf{u}_c \rangle| |\langle \mathbf{u}_d \rangle - \langle \mathbf{u}_c \rangle| \quad (2.16)$$

with ρ_c the density of the continuous phase, A_d the contact area between the droplet and the continuous phase, \mathbf{u}_d and \mathbf{u}_c the velocities of the droplet and continuous phase respectively and C_D the drag coefficient. This drag coefficient is dependent on the Reynolds number of the particle, as calculated in equation 2.17, and the shape of the particle for non-spherical particles. In this thesis, when the 'particle' is mentioned, a dispersed oil droplet is meant. The Reynolds number of the particle is defined as [1]

$$Re_d = \frac{\rho_c D_d (\langle \mathbf{u}_d \rangle - \langle \mathbf{u}_c \rangle)}{\mu_c} \quad (2.17)$$

In equation 2.17 ρ_c and μ_c are the density and the viscosity of the continuous phase respectively. D_d is the diameter of the particle and \mathbf{u}_d and \mathbf{u}_c are the velocities of the particle and continuous phase respectively. The buoyancy force is calculated using the following equation:

$$F_B = \Delta \rho V_d \frac{u_\theta^2}{r} \quad (2.18)$$

$\Delta \rho$ is the density difference between the continuous phase and the oil droplet and V_d is the volume of the oil droplet. The buoyancy force also depends on the azimuthal velocity u_θ and the radial position r .

2.5.2. PARTICLE BREAKUP

As mentioned in section 2.5.1, the main forces that determine the particle trajectory are the buoyancy force and the drag force. The forces depend on V_d and A_d respectively, so both these forces depend on the particle diameter D_d . Therefore the droplet diameter D_d is an important parameter for the separation performance. Particles with a smaller diameter tend to be more difficult to separate, and therefore the separation performance is lower for smaller D_d . Therefore, particle breakup should be avoided for efficient separation. The particle is held together by the interfacial force, which is expressed as [8]

$$F_\sigma = \pi \sigma D \quad (2.19)$$

where σ is the surface tension coefficient between the continuous phase and the oil droplet. D is the droplet diameter. The surface tension force tries to minimize the surface energy. External forces due to fluid-droplet interaction can deform the droplet or break the droplet into smaller droplets. This happens when the external forces acting on the droplet exceed the surface tension force. This can happen for several reasons. [10]

1. The droplet breaks due to local oscillations in pressure or velocity. When the exerted forces due to these oscillations exceed the surface tension of the droplet-fluid interface, the droplet breaks.
2. The droplet breaks due to excess stresses at the surface. This happens when the stress is larger than the surface tension force. This stress is caused by the drag force and viscous stress.
3. The droplet breaks because it is immersed in a strongly accelerating flow.

When the droplet breaks up, the separation efficiency is lowered. Therefore it is important to know when this happens. For the first case, the droplet breaks due to normal stresses caused by pressure fluctuations. This normal stress is expressed as [6]

$$\tau_{ns} = \rho_c \Delta \langle \mathbf{u} \rangle^2 \quad (2.20)$$

This is counteracted by the interfacial stress

$$\tau_{if} = \frac{4\sigma}{D_d} \quad (2.21)$$

The ratio between these forces is given by the Weber number. This is the ratio between the shear force, which tries to break the particle, and the force that tries to keep the particle together.

$$\text{We} \propto \frac{\tau_{ns}}{\tau_{if}} \quad (2.22)$$

Therefore, for high Weber number, the particle is likely to break up and a low Weber number is preferred. For the second case, the ratio between the internal and external viscous stresses is proportional to the viscosity ratio of the fluid and the droplet. In this study this ratio is large, and therefore it is not expected that the droplets will breakup as a result of shear alone. [6] For a high separation efficiency a good balance needs to be found between avoiding droplet breakup and generating enough swirl to drive the particle inward.

2.5.3. PARTICLE COALESCENCE

Apart from droplet breakup, droplet coalescence can also occur. Coalescence can occur when two oil droplets collide [8]. These collisions are more likely to happen when a higher concentration of oil droplets is present in the swirl tube. For this research the inlet concentrations of oil are assumed to be low, and therefore coalescence is unlikely to occur.

2.6. SEPARATION PERFORMANCE

The main objective of this research is to understand how the physical processes in the in-line swirl separator influence the separation performance. This separation performance is defined as the dispersed efficiency, given by:

$$\eta_{\text{dispersed}} = 1 - \frac{\Phi_{\text{water in LPO}} + \Phi_{\text{oil in HPO}}}{\Phi_{\text{tot}}} \quad (2.23)$$

In this equation Φ is the volumetric flux and η is the efficiency, which can take on values between 0 and 1. This efficiency is based on the volumetric flow that ends up in the 'wrong' outlet. For instance, water has a higher density than oil and therefore, when the separator works perfectly, should end up in the Heavy Phase Outlet. Water that ends up in the LPO therefore causes a decrease in efficiency. The same goes for oil ending up in the HPO. From equation 2.23 it can be seen that when no water ends up in the LPO and no oil ends up in the HPO, $\eta_{\text{dispersed}} = 1$. This makes sense, because in that case the oil-water mixture is perfectly separated.

3

BASE MODEL FOR AN IN-LINE SWIRL SEPARATOR

This chapter discusses the base model that was built in a first attempt to describe the physical processes occurring in an in-line liquid-liquid swirl separator. This base model is a mechanistic model, which means that the general picture can be captured by solving the smaller parts that it consists of. The model outline and theory will be explained, as well as the assumptions that are made. Then the results of the model are discussed.

3.1. ASSUMPTIONS

Each model is per definition a simplified representation of reality. Therefore each model is based on certain assumptions. The assumptions that are made for this base model are:

1. The axial component of the velocity field of the continuous phase is assumed to be constant for all radial positions r and all downstream positions z . This is called 'plug flow'. The oil droplet is assumed to move along with the continuous phase in the axial direction.
2. The dispersed oil droplets are assumed to be spherical and rigid: they cannot be deformed or break up due to external forces.
3. For the forces acting upon the oil droplets a quasi-steady state is assumed. This means that the net force acting upon the droplet is zero.
4. Oil droplets are treated as point particles. When the center of the particle ends up inside the collection tube, the droplet is assumed to be collected.
5. Recirculation effects near the collection tube are neglected.
6. The swirling flow is characterized as a Rankine vortex, as described in section 2.3.1. It is assumed that the swirl does not decay downstream and no vortex breakdown occurs.

3.2. MODEL OUTLINE

The general idea of this model is to calculate the separation efficiency for certain key parameters. This model consists of 10 key parameters which altogether fully characterize the system. The key parameters describe the geometry of the system, the vortex, the oil droplet and the continuous phase characteristics. A schematic overview of the in-line swirl separator with the key parameters for the geometry is shown in figure 3.1.

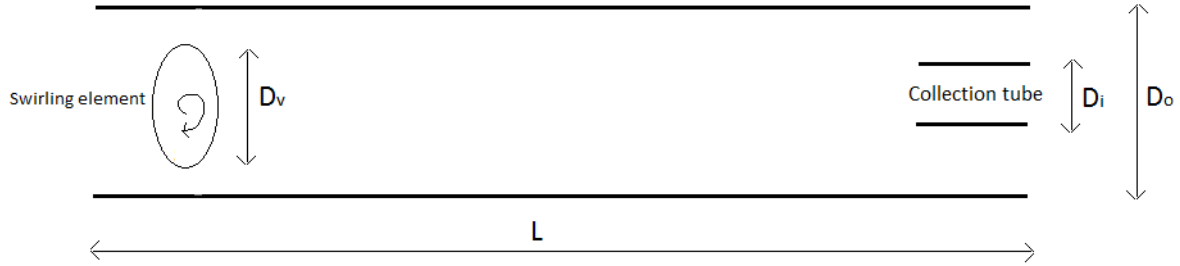


Figure 3.1: Schematic of the in-line swirl separator with the geometry key parameters for the mechanistic model.

The geometry parameters that are shown in figure 3.1 are listed below, along with the other key parameters.

Geometry parameters

- L is the length of the swirl tube in the axial direction.
- D_o is called the 'outer diameter', which is the diameter of the swirl tube.
- D_i is called the 'inner diameter', which is the diameter of the collection tube.

Vortex parameters

- D_v is the core diameter of the vortex, as described in section 2.3.1.
- ω is the vorticity as described in equation 2.7.

Particle parameters

- D_p is the diameter of the particle, which is constant for a rigid particle.
- ρ_p is the density of the particle.

Fluid parameters

- ρ_f is the density of the fluid.
- μ_f is the dynamic viscosity of the fluid.
- U_z is the streamwise velocity of the fluid in m/s. In this model, where plug flow is assumed, this is constant for every radial position r and downstream component z .

Using these key parameters as input for the system and a balance of force, the radial and axial velocity components of the particle are analysed. From these calculations the trajectory of the particle can be reconstructed as schematically illustrated in figure 3.2.

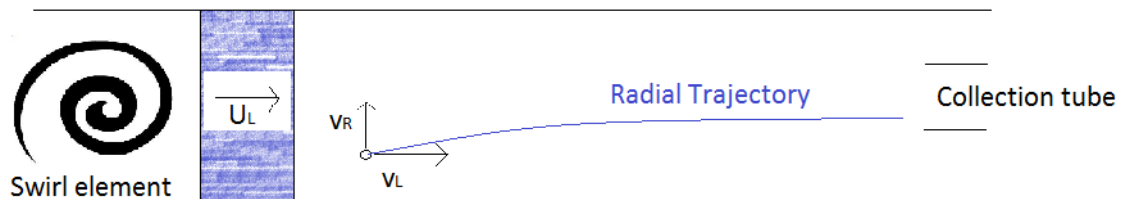


Figure 3.2: Schematic of the radial trajectory of a particle in an in-line swirl separator for the mechanistic model.

Using the radial trajectory of an oil droplet the dispersed efficiency can be determined.

3.3. BALANCE OF FORCES

The core of the mechanistic model is formed by the balance of forces that act upon the dispersed oil droplets. As described in section 2.5.1 the main two forces that determine the particle trajectory are the buoyancy force and the drag force. The buoyancy force is calculated using equation 2.18 and the drag force is calculated as described in equation 2.16. As discussed in section 2.5.1, the drag coefficient C_D is a function of the Reynolds number. Many formulas to express this drag coefficient exist. the expression for the drag coefficient that is being used in this model is as follows [11]:

$$C_D = \frac{24}{\text{Re}} + 0.445 \quad (3.1)$$

In this equation Re is the Reynolds number. This expression for the drag coefficient gives a good approximation for the drag coefficient for large values for the Reynolds number as well as small values for the Reynolds number [11]. For the radial trajectory of the particle, the radial components of the forces acting upon the particle are relevant. The Reynolds numbers used to calculate the drag coefficient in equation 3.1 is the Reynolds number of the particle in the radial direction, which is expressed as:

$$\text{Re}_r = \frac{\rho_f D_p u_r}{\mu_f} \quad (3.2)$$

In this equation u_r is the radial velocity of the particle. In order to find this radial velocity, a balance of forces is used. According to assumption 3 the particle is in a quasi-steady state. Therefore the buoyancy force and the radial component of the drag force must be in equilibrium.

$$F_B = F_D \quad (3.3)$$

$$\Delta\rho V_p \frac{u_\theta^2}{r} = \frac{1}{2} \rho_f C_D A_p u_r^2$$

u_θ is calculated using equation 2.10 for a Rankine vortex. A_p and V_p are the contact area and the volume of the particle respectively. $\Delta\rho$ is the difference in density between the fluid and the particle. Assumption 2 states that the particles are spherical. Therefore A_p and V_p are calculated as

$$A_p = \frac{\pi}{4} D_p^2 \quad (3.4)$$

$$V_p = \frac{\pi}{6} D_p^3 \quad (3.5)$$

By combing equations 3.3, 3.4 and 3.5, the following expression for u_r is found.

$$u_r^2 C_D = \frac{4}{3} D_p \frac{\Delta\rho}{\rho_f} \frac{u_\theta^2}{r} \quad (3.6)$$

By inserting expression 3.1 into equation 3.6 an expression for u_r can be found of the form

$$a u_r^2 + b u_r + c = 0 \quad (3.7)$$

In this equation, the coefficients a , b and c are:

- $a = 0.445$
- $b = \frac{24\mu_f}{\rho_f D_p}$
- $c = -\frac{4}{3} D_p \frac{\Delta\rho}{\rho_f} \frac{u_\theta^2}{r}$

For small Re_r (small u_r) equation 3.7 reduces to

$$bu_r + c = 0 \quad (3.8)$$

as the first term in equation 3.1 will be the leading term for C_D . For large Re_r equation 3.7 will reduce to

$$au_r^2 + c = 0 \quad (3.9)$$

as the second term in equation 3.1 will be the dominant term for C_D . From these coefficients u_r can be calculated using

$$u_r(r) = \frac{-b + \sqrt{b^2 - 4ac}}{2a} \quad (3.10)$$

In this case u_r is a function of r , because $u_\theta = u_\theta(r)$ as well since assumptions 1 and 6 state that the swirl does not decay downstream and the axial velocity component is constant.

3.3.1. SEPARATION EFFICIENCY

By evaluating u_r repetitively at different points in time for small timesteps dt the radial position r of the particle can be calculated as a function of time t . For calculating subsequent radial positions r_n and r_{n+1} the following equation is used:

$$r_{n+1} = r_n + u_{r,n} dt \quad (3.11)$$

In this equation r_{n+1} is the radial position at point $n+1$, r_n is the radial position at point n and $u_{r,n}$ is the radial velocity component at point n . The timestep dt must be small enough such that the for the radial displacement dr that takes place during a timestep dt is much smaller than the radius of the swirl tube. Therefore the following condition must be met.

$$\frac{r(t+dt) - r(t)}{R_o} \ll 1 \quad (3.12)$$

By doing similar calculations for the downstream position of the particle and combining these two results, the radial trajectory of the particle as illustrated in figure 3.2 can be calculated. From these radial trajectory calculations it is possible to determine whether the particle ends up in the collection tube or not. Because this model does not include secondary flow structures, a particle that enters the tube at a smaller radial position r is more likely to be collected in the collection tube than a particle that enters the tube at a larger radial position. The separation efficiency can be determined by evaluating for which radial start position at the beginning of the tube the particle still ends up in the collection tube. This critical radial position $R_{critical}$ is the maximum radial start position for which the particle is collected in the collection tube. For radial start positions $r_{start} > R_{critical}$ the oil droplet ends up outside the collection tube and is therefore not collected. The separation efficiency of the system for given input parameters is calculated as

$$\eta = \left(\frac{R_{critical}}{R_o} \right)^2 \quad (3.13)$$

η is the separation efficiency R_o is the outer radius of the swirl tube ($D_o/2$) and $R_{critical}$ is as explained above.

3.4. NON-DIMENSIONAL ANALYSIS

This section discusses the results that are obtained with this model in non-dimensional form. Displaying the results in non-dimensional form can enhance the understanding of the influence of the different parameters on the separation efficiency.

3.4.1. NON-DIMENSIONAL NUMBERS

This model is characterized by 10 key parameters and 3 basic dimensions: mass, length and time. According to the Buckingham's Π theorem [12] the number of non-dimensional numbers required to fully characterize a system is given by

$$n = p - d \quad (3.14)$$

where n is the number of required non-dimensional numbers, p is the number of key parameters and d is the number of independent dimensions. Using equation 3.14 it is found that for this system 7 non-dimensional

numbers are required. Needless to say, non-dimensional numbers must be dimensionless. Furthermore a set of non-dimensional numbers that characterize the system must be independent. According to the Buckingham's Π theorem the separation efficiency η , which is dimensionless, can be expressed as a multiplication of non-dimensional numbers. By varying one non-dimensional number while keeping all the others constant, the influence of the non-dimensional number on the separation efficiency can be determined. In this research, the following set of non-dimensional numbers has been chosen:

1. $\frac{F_B}{F_I}$. This gives the ratio between the buoyancy force F_B and the inertial forces F_I .
2. Re_r . This is the Reynolds number of the particle based on the radial velocity component of the particle.
3. $\frac{u_\theta}{U_z}$. The ratio between the characteristic azimuthal velocity component of the particle and the axial velocity component.
4. $\left(\frac{D_i}{D_o}\right)^2$
5. $\frac{D_o}{L}$
6. $\frac{D_p}{D_o}$
7. $\frac{D_v}{D_o}$

For non-dimensional number 1, the following derivations are used:

$$F_B \propto \Delta\rho D_p^3 \frac{u_\theta^2}{r} \quad (3.15)$$

As can be derived from equation 2.18. To express u_θ and r in terms of the key parameters, the following relations are used:

$$u_\theta = \omega R_v \quad (3.16)$$

$$r \propto R_v \quad (3.17)$$

Combining relations 3.16 and 3.17 results in

$$\frac{u_\theta^2}{r} \propto \omega^2 R_v \quad (3.18)$$

where R_v is the vortex radius. Combining relations 3.15 and 3.18 finally yields

$$F_B \propto \Delta\rho D_p^3 \omega^2 R_v \quad (3.19)$$

For F_I the following derivations are used:

$$F_I \propto \rho_f D_p^2 u_r^2 \quad (3.20)$$

where u_r is the characteristic radial velocity of the particle that is needed to let the particle end up in the collection tube. Note that this is an estimation for the magnitude of u_r , not the exact value. For this characteristic radial velocity, the following relation is used

$$u_r \propto (D_o - D_i) \frac{U_z}{L} \quad (3.21)$$

Which is an estimation based on the estimated path length ($D_o - D_i$) divided by time it takes to travel along this path ($\frac{L}{U_z}$). Combining relations 3.20 and 3.21 yields

$$F_I \propto \rho_f D_p^2 (D_o - D_i)^2 \frac{U_z^2}{L^2} \quad (3.22)$$

Finally, combining equations 3.19 and 3.22 the first non-dimensional number is expressed in terms of the key parameters:

$$\frac{F_B}{F_I} \propto \frac{\Delta \rho \omega^2 R_v D_p L^2}{\rho_f U_z^2 (D_o - D_i)^2} \quad (3.23)$$

Non-dimensional number 2 is expressed in terms of the key parameters by combining equations 3.2 and 3.21 results in

$$\text{Re}_r \propto \frac{\rho_f D_p (D_o - D_i) U_z}{\mu_f L} \quad (3.24)$$

Non-dimensional number 3 is expressed in terms of the key parameters using relation 3.21. This results in

$$\frac{u_\theta}{U_z} = \frac{\omega R_v}{U_z} \quad (3.25)$$

The derived non-dimensional numbers expressed in terms of the key parameters are listed below.

Non-Dimensional numbers

1. $\frac{F_B}{F_I} \propto \frac{\Delta \rho \omega^2 R_v D_p L^2}{\rho_f U_z^2 (D_o - D_i)^2}$
2. $\text{Re}_r \propto \frac{\rho_f D_p (D_o - D_i) U_z}{\mu_f L}$
3. $\frac{u_\theta}{U_z} = \frac{\omega R_v}{U_z}$
4. $\left(\frac{D_i}{D_o}\right)^2$
5. $\frac{D_o}{L}$
6. $\frac{D_p}{D_o}$
7. $\frac{D_v}{D_o}$

3.5. NON-DIMENSIONAL RESULTS

In this section the relevant results from the non-dimensional analysis will be presented. These results illustrate the influence of the individual non-dimensional numbers on the separation performance. This is done by varying one of these non-dimensional numbers at the time, while keeping all the others constant. The constant values of the non-dimensional numbers are given in table 3.1. Standard values that are used for the key parameters are the same as for the comparison with experimental results, as given in table 3.2. The relevant non-dimensional results will be presented below, the other results can be found in appendix A.

$$\begin{array}{ll} \frac{F_B}{F_I} = 2.8 & \left(\frac{D_i}{D_o}\right)^2 = 0.25 \\ \frac{u_\theta}{U_z} = 1.9 & \text{Re}_r = 5.3 \\ \frac{D_o}{L} = 0.06 & \frac{D_p}{D_o} = 10^{-3} \\ \frac{D_v}{D_o} = 0.5 & \end{array}$$

Table 3.1: The standard values for the non-dimensional numbers as used in the non-dimensional analysis.

3.5.1. BUOYANCY FORCE VS. INERTIAL FORCES

The first non-dimensional number gives the ratio between the buoyancy force F_B and the inertial forces F_I . The buoyancy force drives the particle radially inward, whereas the inertial force is pointed radially outward. The influence of this ratio while all other non-dimensional numbers are kept constant at the values shown in table 3.1 is shown in figure 3.3.

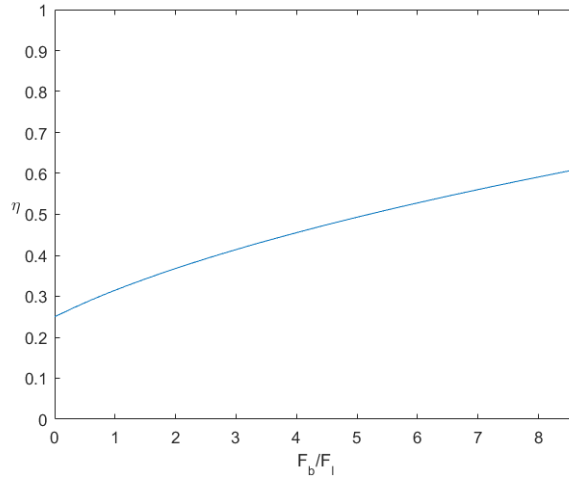


Figure 3.3: The influence of the non-dimensional number $\frac{F_B}{F_I}$ on the separation efficiency. All other non-dimensional numbers are kept constant and equal to the values in table 3.1.

Figure 3.3 shows that for increasing $\frac{F_B}{F_I}$ the efficiency increases. This is expected, because the buoyancy force drives the particle radially inwards, which results in a higher efficiency. As can be seen, the efficiency $\eta = 0.25$ for $\frac{F_B}{F_I} = 0$. This makes sense, because when the buoyancy force is absent, the radial velocity of the particle $u_r = 0$, as can be seen from equation 3.3. When the radial velocity is zero, the radial position of the particle will be the same at the end of the swirl tube as at the beginning. In this experiment $\frac{D_i}{D_o} = 0.5$ as can be found in table 3.2. Therefore the flow split will be constant at $FS = 0.25$ as can be calculated from equation 2.15. Therefore $\eta = 0.25$ is expected for $\frac{F_B}{F_I} = 0$.

3.5.2. RADIAL REYNOLDS NUMBER

The results for varying the Reynolds number of the particle based on the radial velocity component of the particle, non-dimensional number 2, are shown in figure 3.4.

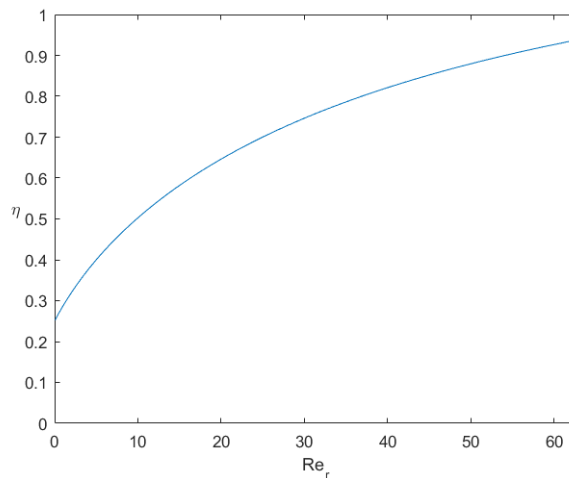


Figure 3.4: The influence of the non-dimensional number Re_r on the separation efficiency. All other non-dimensional numbers are kept constant and equal to the values in table 3.1.

The results shown in figure 3.4 show similar results as for figure 3.3. A larger Re_r is usually related to a higher u_r and therefore results in a higher efficiency. For similar reasons as described in the previous section, $\eta = 0.25$ for $Re_r = 0$.

3.5.3. CONSISTENCY OF NON-DIMENSIONAL RESULTS

The results shown in sections 3.5.1 and 3.5.2 are for varying a non-dimensional number while keeping the other non-dimensional numbers constant at the values shown in table 3.1. This section discusses how these results would change when different values for these non-dimensional numbers would be used. In all cases, the general trend for varying non-dimensional numbers will be unchanged by the values of the non-dimensional numbers that are kept constant. Changing these values will merely result in a shift of the efficiency curves. For instance, it can be seen in figures 3.3 and 3.4 that $\eta = 0.25$ for $\frac{F_B}{F_I} = 0$ and $Re_r = 0$ respectively. This is because the standard value of $(\frac{D_i}{D_o})^2 = 0.25$ is used as shown in table 3.1. When a different value for this non-dimensional number would be used, the efficiency at $\frac{F_B}{F_I} = 0$ and $Re_r = 0$ would change. For example, if $(\frac{D_i}{D_o})^2 = 0.36$, then the efficiency curves in figures 3.3 and 3.4 would start at $\eta = 0.36$.

For larger values of $\frac{F_B}{F_I}$, the efficiency increases at a higher rate. Therefore the curve in figure 3.4 would start at the same value of η , but the slope of the curve would be steeper for larger values of $\frac{F_B}{F_I}$. For smaller values of $\frac{F_B}{F_I}$ the opposite happens. When using a larger value for Re_r , $\frac{u_\theta}{U_z}$ and $\frac{D_v}{D_o}$ the efficiency curve changes in a similar way as for increasing $\frac{F_B}{F_I}$.

Increasing the value of $\frac{D_o}{L}$ generally results in a smaller increase in efficiency. Using different values for $\frac{D_p}{D_o}$ does not result in a change in efficiency, although the absolute value of D_p does play an important role in the separation efficiency, as will be shown in section 3.6.2.

3.6. PARAMETER INFLUENCE

This section discusses the influence of the different parameters on the separation performance. For these calculations the parameters from Slot [1] have been used, which are listed in table 3.2, unless mentioned that a different value is used.

L	=	1.70 m	μ_f	=	$1.183 \cdot 10^{-3}$ Pa.s
D_o	=	0.1 m	ρ_f	=	1067.8 kg/m ³
D_i	=	0.05 m	ρ_p	=	881 kg/m ³
D_v	=	0.05 m	D_p	=	100 μ m
U_z	=	2.0 m/s	ω	=	100 s ⁻¹

Table 3.2: The standard values for the key parameters that are used for the numerical simulations. Values from Slot [1].

3.6.1. VORTICITY

The vorticity ω determines the strength of the swirl and therefore the azimuthal velocity of the particle u_θ . The separation efficiency as a function of ω is shown in figure 3.5. For these calculations the parameters of table 3.2 are used, except that ω has been varied.

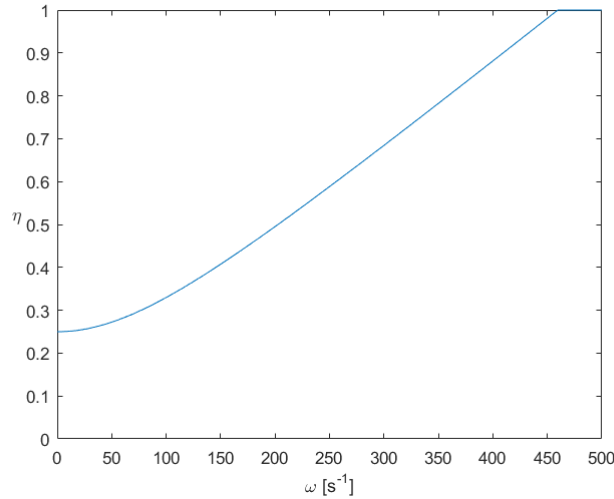


Figure 3.5: The influence of ω on the separation efficiency η of the base model.

In this figure η is the separation efficiency. As can be seen in in figure 3.5, the separation efficiency increases for increasing ω . This was expected, because for increasing ω section 2.3.1 shows that u_θ increases for a Rankine vortex. Therefore u_r increases as well, which results in a higher η . For large values of ω the efficiency increases towards 1. From the figure can also be concluded that for $\omega = 0$ the value $\eta = 0.25$ is found. This makes sense, because for $\omega = 0$ it is expected that $u_r = 0$ and that the radial position of the particle at the end of the swirling tube does not differ from the radial position at the beginning. Since $D_i/D_o = 0.5$, as can be seen in table 3.2, this results in an efficiency of $\eta = (0.5)^2 = 0.25$. For values of ω larger than 150 s^{-1} the efficiency increases near-linearly for increasing ω .

3.6.2. PARTICLE DIAMETER

The particle diameter D_p influences the strength of the buoyancy force driving the particle inwards, as can be seen in equation 2.18. A larger buoyancy force increases u_r and therefore the separation efficiency is expected to increase as well. The separation efficiency as a function of D_p is shown in figure 3.6. For these calculations the parameters of table 3.2 are used, except that D_p has been varied.

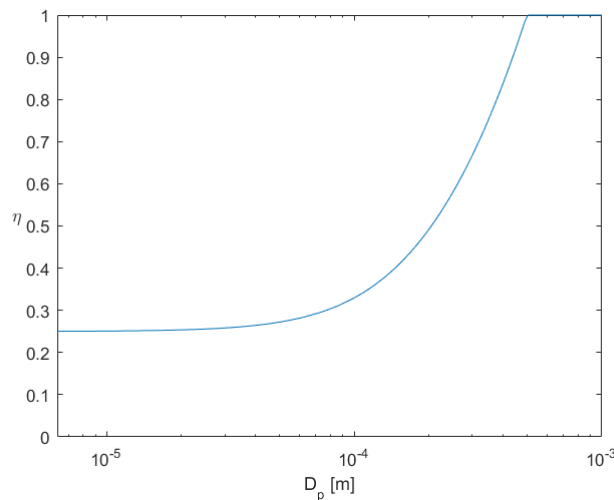


Figure 3.6: The influence of the particle diameter D_p on the separation efficiency η of the base model.

From figure 3.6 it can be concluded that the particle diameter D_p plays an important role in the separation performance. For small D_p the value $\eta = 0.25$ is found. This is expected, because for small D_p the buoyancy force is small and therefore u_r is small as well. Therefore for $D_i/D_o = 0.5$ this efficiency value is expected as

explained in section 3.6.1. From values for the particle diameter of $D_p = 10^{-4}$ and up the separation efficiency increases dramatically. This observation could be interesting for the development of a more sophisticated model.

These results correspond with the non-dimensional results discussed in section 3.5 because $F_B \propto D_p^3$ and for increasing F_B the efficiency increases. Also $Re_r \propto D_p$ and an increasing Re_r leads to increasing efficiency as explained in section 3.5.

3.7. CONCLUSIONS

Based on the results from the base model, some conclusions can be drawn. According to the base model:

1. When keeping all other non-dimensional numbers constant and increasing $\frac{F_B}{F_I}$, the efficiency increases.
2. When keeping all other non-dimensional numbers constant and increasing Re_r , the efficiency increases.
3. The separation efficiency is strongly dependent on the particle diameter D_p .
4. Increasing the vorticity ω results in a higher separation efficiency.

It must be emphasized that these conclusions are based on the findings from the base model. These conclusions will be tested in the following chapters.

4

BASE MODEL COMPARISON WITH CFD AND EXPERIMENTS

In this chapter the base model as described in chapter 3 will be compared to Computational Fluid Dynamics (CFD) results from Slot [1] and experimental results from Van Campen [2]. Based on this comparison conclusions will be drawn for the extent to which the base model represents reality and which aspects should be improved in a more sophisticated model.

4.1. COMPARISON WITH CFD

This section describes the comparison of the base model described in chapter 3 to the results from CFD simulations by Slot. These CFD simulations essentially come down to the principle as the base model, which is calculating the flow fields in the swirl separator. However, where the base model is built on many assumptions to simplify the situation, the CFD simulations are complicated and describe the flow fields in a sophisticated way. Like the base model, the CFD simulations by Slot do not take droplet breakup and coalescence into account. Therefore the droplets are assumed to have a constant diameter. Slot has done CFD simulations for different swirl strengths. The strength of the swirl is characterized by Slot [1] by the swirl angle Sw .

$$Sw = \frac{u_{\theta,te}}{u_z} \quad (4.1)$$

$u_{\theta,te}$ is the azimuthal velocity at the trailing edge of the swirling element's vanes. u_z is the axial velocity of the fluid. To compare the results from the base model to the results from CFD, the model needs to be tested under the same circumstances as they were during the simulations. In this section the results from CFD simulations by Slot for strong swirling will be used. According to Slot $Sw = 6.72$ for strong swirling. The input values for the key parameters that were used by Slot are given in table 4.1.

L	$=$	1.70 m	μ_f	$=$	$1.183 \cdot 10^{-3}$ Pa.s
D_o	$=$	0.1 m	ρ_f	$=$	1067.8 kg/m ³
D_i	$=$	0.05 m	ρ_p	$=$	881 kg/m ³
U_z	$=$	2.0 m/s	D_p	$=$	100 μ m

Table 4.1: The standard values for the key parameters that are used for the numerical simulations when comparing the base model to CFD simulations by Slot. Values from Slot [1].

The only key parameters that are missing in this table are ω and D_v , the vorticity and the diameter of the vortex core respectively. The values for ω and D_v can be determined from simulations of the azimuthal velocity u_θ by Slot. To find these values the azimuthal velocity profile of a Rankine vortex, which is described in section 2.3.1, has to be fitted to the data of the simulated u_θ profile by Slot. From Slot's simulations, different combinations of ω and D_v can be obtained and tested to see whether the resulting calculated efficiencies correspond to the efficiencies obtained by Slot. The velocity fields at different downstream positions z as given in figures 4.1 and 4.2 are obtained by Slot by simulating for strong swirling. It must be noted that these

simulations were done for a flow split of $FS = 0.30$ whereas the base model uses $FS = 0.25$. However, this is the closest flow split value that could be compared with and the differences due to the flow split difference are marginal. These marginal difference will not be significant to this comparison, as the main goal of this comparison is to get an impression of roughly how well the base model approximates the CFD results. The comparison of the simulated azimuthal velocity fields and the fitted Rankine vortex velocity fields can be found in figures 4.1 and 4.2.

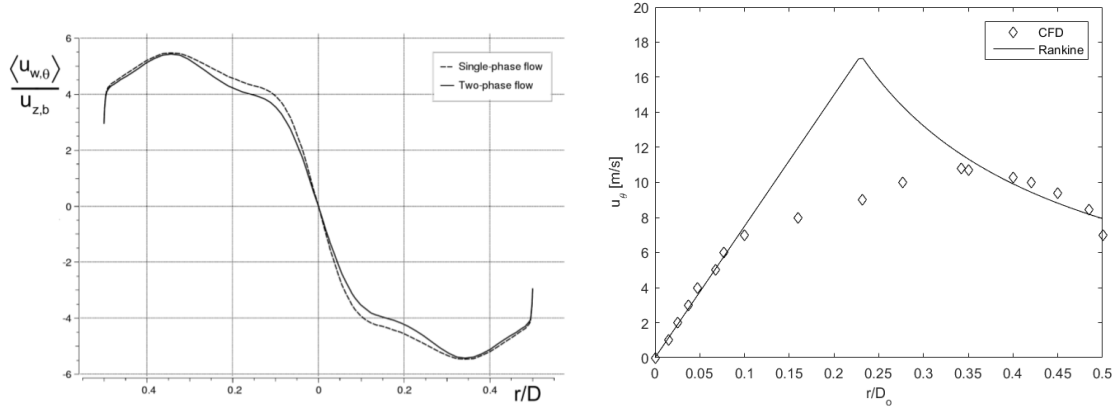


Figure 4.1: On the left: The azimuthal velocity field at $z = 0.50\text{m}$ as simulated by Slot for strong swirling and $FS = 0.30$. On the right: the azimuthal velocity profile of a Rankine vortex fitted to the experimental CFD data from Slot [1].

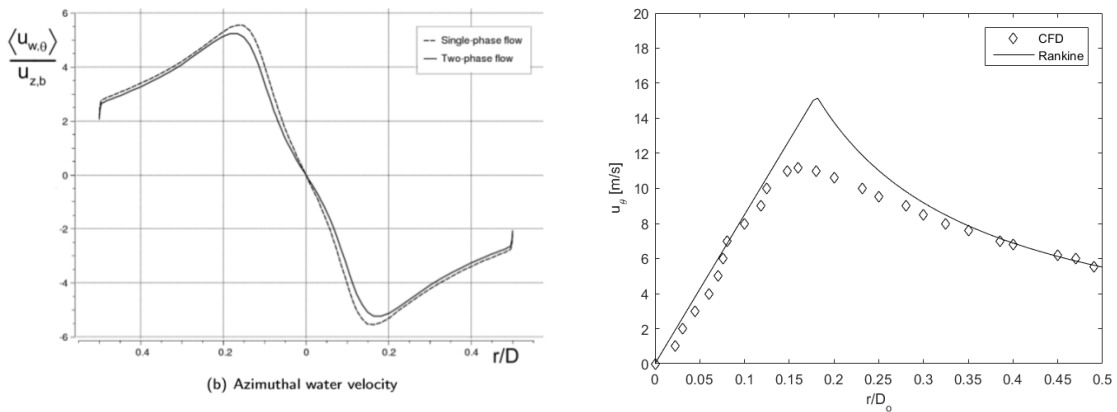


Figure 4.2: On the left: The azimuthal velocity field at $z = 1.50\text{m}$ as simulated by Slot for strong swirling and $FS = 0.30$. On the right: the azimuthal velocity profile of a Rankine vortex fitted to the experimental CFD data from Slot [1].

Figures 4.1 and 4.2 show that, especially at $z = 0.50\text{m}$, the Rankine vortex velocity profile does not fit the simulated velocity profile well. Especially at $z = 1.50\text{m}$ the azimuthal velocity profile seems to resemble a Gaussian vortex quite well, as can be seen in figure 6.1. From the fitted Rankine vortex profiles ω and D_v at $z = 0.50\text{m}$ and $z = 1.50\text{m}$ are found. Using that the swirl angle for strong swirling is $Sw = 6.72$, the input of table 4.1 and the value for the radial position of the trailing edge of the vane of the swirling element $r_{te} = 0.045\text{m}$, ω and D_v for $z = 0\text{m}$ can be calculated. The values for the fitted and calculated parameters ω and D_v for different z are shown in table 4.2.

z [m]	ω [s^{-1}]	D_v [m]
0.0	597	0.090
0.5	1500	0.046
1.5	1580	0.030

Table 4.2: The values for ω and D_v that are obtained by fitting a Rankine vortex profile to results from simulations by Slot [1]. These simulations are for strong swirling, $Sw = 6.72$.

Table 4.2 shows that the vorticity and vortex diameter are not, as assumed in the base model, constant over the length of the swirl tube. However, it is more important to check whether the strength of the vortex changes significantly as a function of z . To investigate this, the circulation Γ is calculated for the different z positions using equation 2.8 and the parameters from table 4.2. The results are shown in table 4.3.

z [m]	Γ [m ² /s]
0.0	3.82
0.5	2.57
1.5	1.69

Table 4.3: The values for the circulation Γ that are calculated for different positions z using results from simulations by Slot [1]. These simulations are done for strong swirling, $Sw = 6.72$.

Table 4.3 shows that according to the CFD simulations the strength of the vortex decays significantly along the length of the swirl tube. Slot found that the loss in angular momentum was approximately 46% over a pipe length of $L = 10D_o$ [1]. Equation 2.4 shows that the swirl number is a measure of the flux of angular momentum. The circulation Γ is similar to the angular momentum. From equations 2.4 and 2.9 it can be seen that the circulation decays similar to the swirl number. Therefore, using equation 2.5 the decay of circulation can be defined as

$$\Gamma(z) = \Gamma_0 e^{-C_{dc} \frac{z-z_0}{D}} \quad (4.2)$$

where Γ_0 is the circulation at $z = 0$. From table 4.2 it is clear that the diameter of the vortex core decays downstream. However, when assuming this diameter to be constant, the same C_{dc} can be used for the circulation and the swirl number. As mentioned before, this decay is similar to the decay in angular momentum. Therefore, by using the decay of 46% over $L = 10D_o$ the value for the decay constant is determined to be $C_{dc} = 0.0616$. This decay constant is used to compare the circulation decay with the circulation values of table 4.3. The results are displayed in figure 4.3.

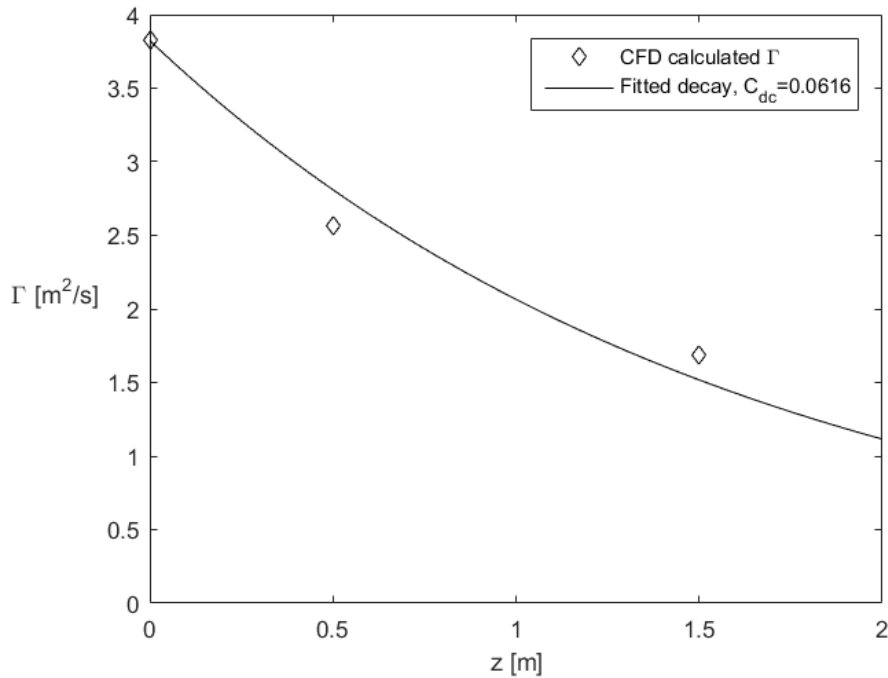


Figure 4.3: The decay of circulation Γ based on simulations by Slot [1] as a function of z for strong swirling. The solid line is the decaying circulation for $C_{dc} = 0.0616$

As figure 4.3 shows, the swirl decay coefficient value of $C_{dc} = 0.0616$ seems to result in a good approximation of the swirl decay.

When comparing the separation efficiency results of the CFD simulations to the results of the base model, the same input parameters should be used. Therefore the values of table 4.1 are used. Note that the CFD simulations assume a constant droplet size $D_p = 100\mu\text{m}$. For these input parameters and strong swirling the CFD simulations predict an efficiency of $\eta = 0.86$ [1]. When using the parameter values for ω and D_v from table 4.3 the base model predicts $\eta = 1$ for the $z = 0.0\text{m}$, $z = 0.50\text{m}$, $z = 1.50\text{m}$ cases. Since it is now clear that the circulation decay is significant, it makes sense that the base model, which assumes no decay, predicts higher efficiencies than the CFD. However, even when using the values for ω and D_v at $z = 1.50\text{m}$, the efficiency is calculated as $\eta = 1$. Therefore it can be concluded that the base model generally predicts higher efficiencies than the CFD simulations. When using the vortex diameter at $z = 0.0\text{m}$ from table 4.2, the base model requires $\omega = 186\text{s}^{-1}$ to find the efficiency of $\eta = 0.86$ as calculated by Slot. This value for ω is significantly smaller than the value $\omega = 597\text{s}^{-1}$ as given in table 4.2. When assuming that the swirl decays downstream with $C_{dc} = 0.0616$, the vorticity at the end of the swirl tube would be $\omega = 210\text{s}^{-1}$. Even this value is still larger than the ω that is required at the beginning of the swirl tube to reach $\eta = 0.86$. Therefore the swirl decay can only partially account for the difference in efficiency between the base model and the CFD calculations.

4.2. COMPARISON WITH EXPERIMENTAL RESULTS

This section compares the results from the base model to the experimental results from van Campen [2]. For the best possible comparison, the results from the CFD will also be compared to the experimental results, because the CFD is based on similar conditions as the base model. A comparison between efficiencies from CFD simulations and experimental results for strong swirling is shown in figure 4.4.

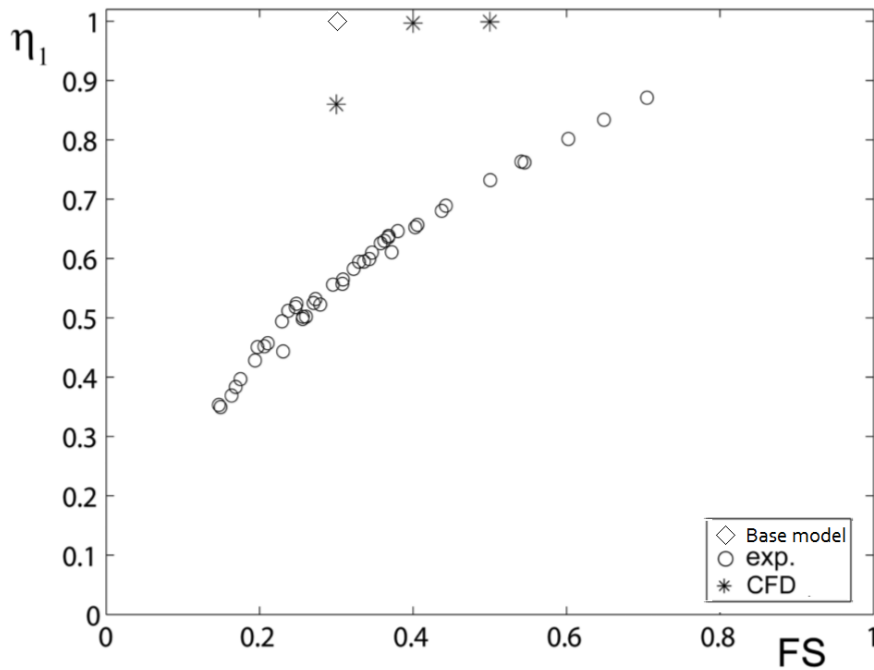


Figure 4.4: Comparison between efficiencies calculated using CFD simulations [1], experimental results from van Campen [2] and the base model for strong swirling at different FS values.

Figure 4.4 shows that the CFD simulations and the base model calculate a significantly higher efficiency than the experimental values. Therefore it can be disputed that the assumptions that are used for the CFD are the correct approach for this problem. The essential difference between the base model and the CFD being the level of sophistication in the flow field, it can be concluded that improving the flow field will not result in efficiency values that are close to the experimental values. The results from the base model as presented in chapter 3 predict the particle diameter D_p to have a large influence on the efficiency. In the CFD simulations and the base model, it is assumed that all particles have $D_p = 100\mu\text{m}$. Since the CFD and base model give higher efficiencies than the experimental results for strong swirling, it should be investigated whether $D_p = 100\mu\text{m}$ is a realistic value for strong swirling. This will be addressed in chapters 5 and 6.

4.3. CONCLUSIONS

From the comparison of the base model to CFD simulations and experimental results some conclusions can be drawn regarding the performance of the base model.

1. The swirl decay should be taken into account when improving the base model. From the circulation decay it was found that a decay efficient of $C_D = 0.0616$ resulted in a decent approximation of this swirl decay as illustrated in figure 4.3.
2. The simulated azimuthal velocity profiles from the CFD simulations show that a Gaussian vortex profile would give a better approximation of the velocity profile. This is especially the case for the simulated azimuthal velocity profile at $z = 1.50\text{m}$ as shown in figure 6.1.
3. Both the CFD and the base model calculate efficiencies significantly larger than the experimental results. The simplified flow field in the base model cannot be the main reason for the aberration in efficiency that is observed between the base model and experimental results, since the main difference between CFD and the base model is the sophistication of the flow field.
4. The particle diameter has a large influence on the efficiency. Therefore it should be investigated whether $D_p = 100\mu\text{m}$ is a realistic value for strong swirling, as both the CFD and the base model calculate efficiencies significantly higher than the experimental values.

5

SWIRL DECAY MODEL

This chapter discusses the improved model that was built to describe the physical processes occurring in an in-line liquid-liquid separator. This new model, which from now on will be referred to as the swirl decay model, is built on the foundation of the base model described in chapter 3. However, some changes have been made with respect to the base model which are based on the conclusions drawn in section 4.3. The swirl decay model resembles the base model in many ways and most of the assumptions remain the same.

5.1. ASSUMPTIONS

The assumptions underlying this model are listed below. Although some are the same as for the base model, the full list of assumptions is given to prevent ambiguity.

1. The axial component of the velocity field of the continuous phase is assumed to be constant for all radial positions r and all downstream positions z . This is called 'plug flow'. The oil droplet is assumed to move along with the continuous in the axial direction.
2. The dispersed oil droplets are assumed to be spherical and rigid: they cannot be deformed or break up due to external forces.
3. For the forces acting upon the oil droplets a quasi-steady state is assumed. This means that the net force acting upon the droplet is zero.
4. Oil droplets are treated as point particles. When the center of the particle ends up inside the collection tube, the droplet is assumed to be collected.
5. Recirculation effects near the collection tube are neglected.
- 6. The swirling flow is characterized as a Gaussian vortex, as described in section 2.3.2.**
- 7. The swirl decays downstream as described in section 2.2.1. The swirl decay coefficient C_{dc} is introduced as a key parameter. Although the swirl decays, the vortex diameter D_v stays constant and no vortex breakdown occurs.**

These assumptions are similar to the assumptions of the base model, except for assumptions 6 and 7. These assumptions back the improvements that are made with respect to the base model.

5.2. MODEL OUTLINE

The outline of the swirl decay model is the same as for the base model, which is described in section 3.2. The only real difference is that a new key parameter is added: the swirl decay coefficient C_{dc} . The new list of key parameters is given below.

Geometry parameters

- L is the length of the swirl tube in the axial direction.
- D_o is called the 'outer diameter', which is the diameter of the swirl tube.
- D_i is called the 'inner diameter', which is the diameter of the collection tube.

Vortex parameters

- D_v is the core diameter of the vortex, as described in section 2.3.1.
- ω is the vorticity as described in equation 2.7.
- C_{dc} is the swirl decay constant, as described in section 2.2.1.

Particle parameters

- D_p is the diameter of the particle, which is constant for a rigid particle.
- ρ_p is the density of the particle.

Fluid parameters

- ρ_f is the density of the fluid.
- μ_f is the dynamic viscosity of the fluid.
- U_z is the streamwise velocity of the fluid in m/s. In this model, where plug flow is assumed, this is constant for every radial position r and downstream component z .

Using these key parameters, the separation efficiency of the swirl separator is calculated. The balance of forces that is used is the same as for the base model. This can be found in section 3.3.

5.3. PARAMETER INFLUENCE

This section is similar to section 3.6, except that for the input parameters more realistic values are used. For instance values for D_p are used that were found during experiments done by van Campen [2]. By using these values this parameter influence analysis will give more realistic results rather than just showing the general influence of the individual parameters. The standard input parameters are listed in table 5.1. These values for ω and D_v correspond to strong swirling. These are the input values that are used in the following parameter analysis, unless mentioned otherwise. From the key parameters two parameters are particularly interesting to study. These are the swirl decay coefficient C_{dc} , which is newly introduced in this model, and the particle diameter D_p , which is expected to have a large influence as seen in section 3.6. Also the dependence on $\frac{L}{U_z}$ proves to be interesting. The experimental results from van Campen [2] show that a particle diameter of $D_p = 50\mu\text{m}$ is a more realistic value for strong and weak swirling than the value of $D_p = 100\mu\text{m}$ which was assumed earlier. Therefore this value will be used as standard value for this parameter. The influence of the key parameters D_p , C_{dc} and $\frac{L}{U_z}$ will be shown for two cases: strong swirling and weak swirling. The influence of the other parameters can be found in Appendix B.

L	=	1.70 m	μ_f	=	$1.183 \cdot 10^{-3}$ Pa.s
D_o	=	0.1 m	ρ_f	=	1067.8 kg/m^3
D_i	=	0.05 m	ρ_p	=	881 kg/m^3
D_v	=	0.09 m	D_p	=	$50 \mu\text{m}$
U_z	=	2.0 m/s	ω	=	500 s^{-1}
C_{dc}	=	0.0616			

Table 5.1: The standard values for the key parameters that are used for the numerical simulations. These parameters correspond to a situation with strong swirling. Values from Slot [1].

5.3.1. STRONG SWIRLING

Strong swirling is characterized by $\omega = 500\text{s}^{-1}$. Figures 5.1 and 5.2 show the dependency of η on D_p and C_{dc} for strong swirling.

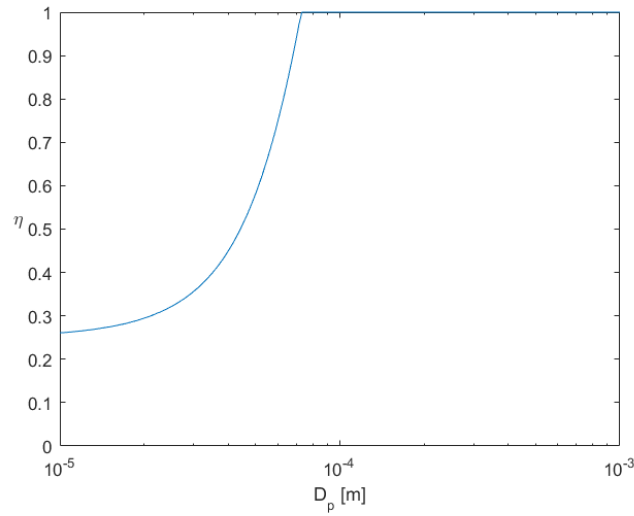


Figure 5.1: The influence of the particle diameter D_p on the separation efficiency for the swirl decay model for strong swirling. The values of the other key parameters are given in table 5.1.

Figure 5.1 shows that for strong swirling and the input parameters of table 5.1 the efficiency η depends strongly on the particle diameter D_p as expected. It can also be seen that the efficiency starts to increase strongly around $D_p = 40\mu\text{m}$. At $D_p = 100\mu\text{m}$ the efficiency has reached a value of 1. So indeed, the previously assumed value for the particle diameter of $D_p = 100\mu\text{m}$ seems to be too large and $D_p = 50\mu\text{m}$ seems to be a more realistic value. Figure 5.2 shows the effect of the newly introduced parameter C_{dc} on the separation performance.

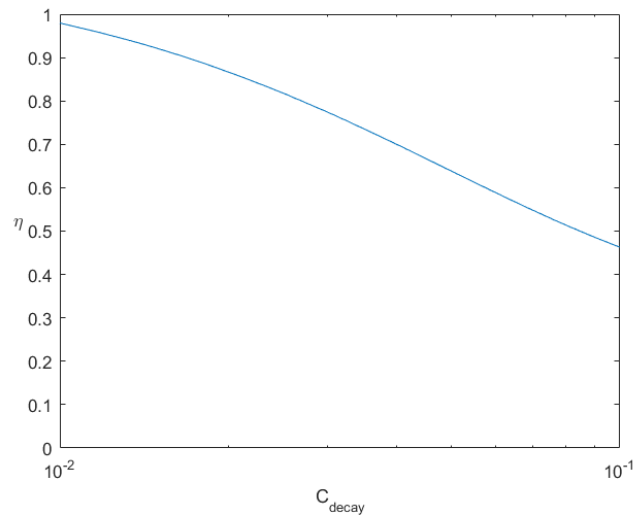


Figure 5.2: The influence of the swirl decay coefficient C_{dc} on the separation efficiency for the swirl decay model for strong swirling. The values of the other key parameters are given in table 5.1.

As can be seen in figure 5.2 the swirl decay coefficient has a significant effect on the separation performance. Realistic values for the swirl decay coefficient range from $0.01 < C_{dc} < 0.1$ [7]. As shown in figure 5.2 this accounts for a difference in separation efficiency of approximately 50%. Therefore it seems to be important to determine C_{dc} as accurately as possible.

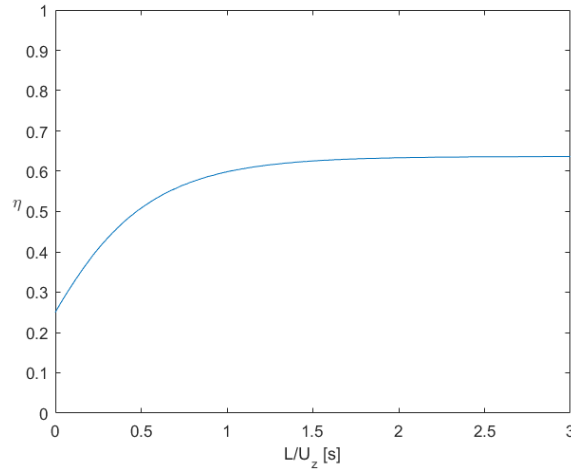


Figure 5.3: The influence of the ratio between the tube length L and the axial velocity U_z on the separation efficiency for the swirl decay model for strong swirling. The values of the other key parameters are given in table 5.1.

Figure 5.3 shows that the efficiency η increases asymptotically as a function of $\frac{L}{U_z}$. This means that at some point, the efficiency is maxed out for these particular input values for the key parameters. As can be seen, for this strong swirling case the efficiency only increases marginally after $\frac{L}{U_z} = 1$. After this, increasing the pipe's length L does not contribute to a higher separation efficiency anymore. This is because the swirl decays as a function of z , so at some point the swirl has become so weak that it does not manage to drive the particle radially inwards anymore. For increasing L to large values, the circulation will decay to approximately 0 at some point. When this happens, the particle will not experience a buoyancy force radially inwards anymore. Because the concentration of oil at the center of the pipe will be higher than in the outer regions, the oil may start traveling radially outwards again due to diffusion phenomena. This could eventually decrease the separation efficiency again.

5.3.2. WEAK SWIRLING

This section will discuss the influence of the same parameters as the previous section for weak swirling. Weak swirling is characterized by an azimuthal velocity of approximately $u_\theta = 8\text{m/s}$ at the trailing edge of the vanes of the swirling element. Therefore this corresponds to $\omega = 360\text{s}^{-1}$. For this section, this value for ω will be used instead of the value listed in table 5.1. The influence of D_p is shown in figure 5.4.

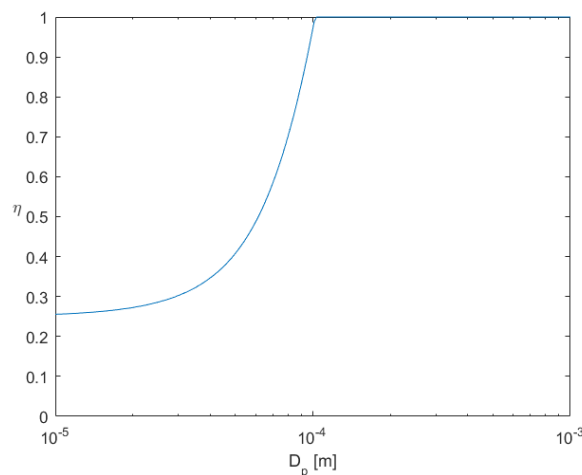


Figure 5.4: The influence of the particle diameter D_p on the separation efficiency for the swirl decay model for weak swirling. The values of the other key parameters are given in table 5.1.

Figure 5.4 shows a similar dependence of η on the particle diameter D_p for weak swirling as shown for strong

swirling in figure 5.1. This shows that for weak swirling the efficiency is strongly dependent on D_p as well. However, when comparing figure 5.4 to figure 5.1, it is noticeable that for weak swirling the efficiency start to rise for a larger value of D_p than for the strong swirling. For weak swirling, the efficiency starts to increase rapidly for $D_p > 50\mu\text{m}$, while for strong swirling this already happened at $D_p > 40\mu\text{m}$. Therefore, when D_p is kept constant, strong swirling will result in a higher efficiency than weak swirling.

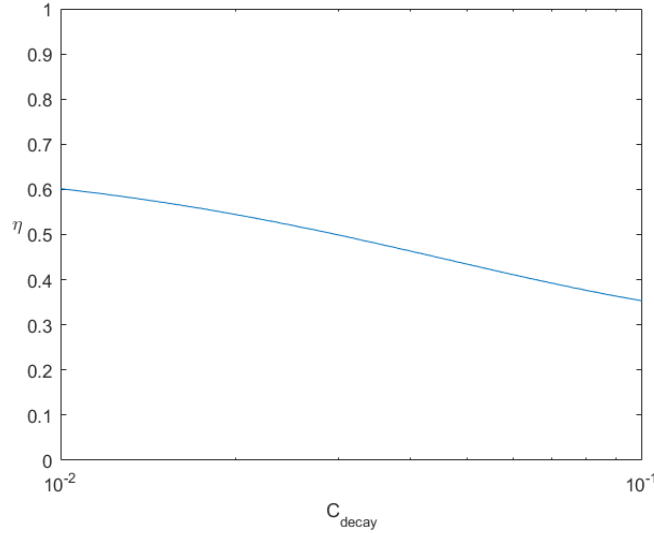


Figure 5.5: The influence of the swirl decay coefficient C_{dc} on the separation efficiency for the swirl decay model for weak swirling. The values of the other key parameters are given in table 5.1.

As can be seen in figure 5.5 the swirl decay coefficient has a significant effect on the separation performance. Realistic values for the swirl decay coefficient range from $0.01 < C_{dc} < 0.1$ [7]. As shown in figure 5.5 this accounts for a difference in separation efficiency of approximately 25%. This is a lower absolute percentage than for strong swirling, although for $C_{dc} = 0.1$ the efficiency has been reduced by 50% with respect to the efficiency at $C_{dc} = 0.01$. Therefore, for weak swirling it can also be concluded that the C_{dc} value should be determined carefully for the best possible result.

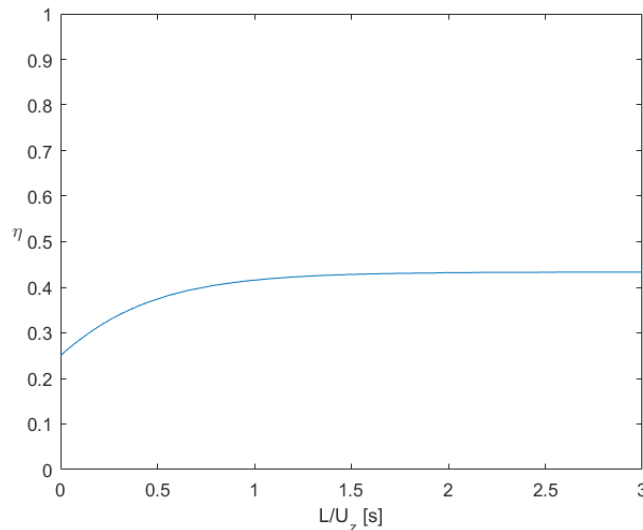


Figure 5.6: The influence of the ratio between the tube length L and the axial velocity U_z on the separation efficiency for the swirl decay model for weak swirling. The values of the other key parameters are given in table 5.1.

Figure 5.6 shows that the influence of $\frac{L}{U_z}$ is the same for weak swirling as for strong swirling.

5.4. CONCLUSIONS

Based on the results from the swirl decay model, some conclusions can be drawn. According to the swirl decay model:

1. The separation efficiency depends strongly on the particle diameter D_p . For strong and weak swirling the efficiency starts to increase strongly around D_p values of $D_p = 40\mu\text{m}$ and $D_p = 50\mu\text{m}$ respectively. This is a significantly smaller value than the previously assumed standard value of $D_p = 100\mu\text{m}$.
2. At some point increasing L does not result in a higher efficiency anymore. This is due to swirl decay. At some point the circulation will become 0 due to this decay, at which point the inward radial velocity of the oil particle will become 0 as well and the efficiency stops increasing. Due to diffusion increasing L beyond a certain point may even decrease the separation efficiency.
3. Realistic swirl decay coefficients of $0.01 < C_{dc} < 0.1$ significantly influence the efficiency of the swirl separator. Therefore C_{dc} should be determined as accurately as possible for the best possible result.

6

SWIRL DECAY MODEL COMPARISON WITH CFD AND EXPERIMENTS

In this chapter the swirl decay model as described in chapter 5 will be compared to Computational Fluid Dynamics (CFD) results from Slot [1] and experimental results from Van Campen [2]. Based on this comparison conclusions will be drawn for the extent to which the swirl decay model represents reality and which aspects should be improved in a more sophisticated model.

6.1. COMPARISON TO CFD

This section describes the comparison of the base model described in chapter 3 to the results from CFD simulations by Slot. To compare the swirl decay model and the CFD simulations accordingly, the same input values should be used. The standard input values for the key parameters are given in table 6.1. These values are for strong swirling.

L	$=$	1.70 m	μ_f	$=$	$1.183 \cdot 10^{-3}$ Pa.s
D_o	$=$	0.1 m	ρ_f	$=$	1067.8 kg/m ³
D_i	$=$	0.05 m	ρ_p	$=$	881 kg/m ³
U_z	$=$	2.0 m/s	D_p	$=$	100 μ m
D_v	$=$	0.09 m	ω	$=$	588 s ⁻¹

Table 6.1: The standard values for the key parameters that are used for the numerical simulations when comparing the base model to CFD simulations by Slot. Values from Slot [1].

The swirl decay coefficient is assumed to be constant at $C_{dc} = 0.0616$ as described in section 4.1. As concluded in section 4.1 the azimuthal velocity profile at $z = 1.50$ m as simulated by Slot resembles a Gaussian vortex, which is illustrated in figure 6.1.

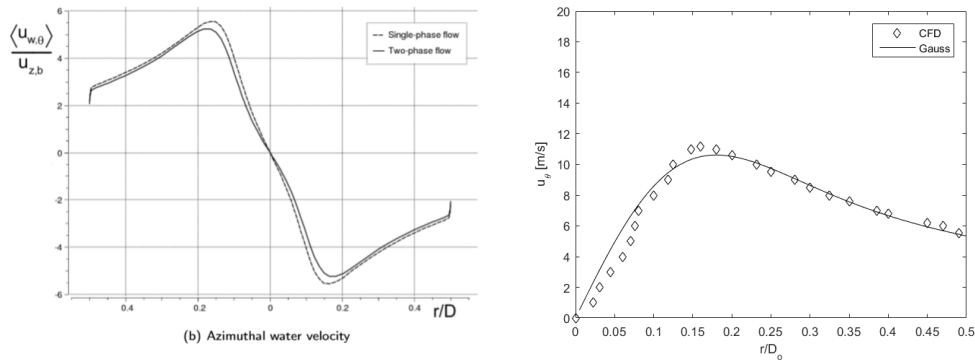


Figure 6.1: On the left: The azimuthal velocity field at $z = 1.50$ m as simulated by Slot for strong swirling and $FS = 0.30$. On the right: the azimuthal velocity profile of a Gaussian vortex fitted to the experimental CFD data from Slot [1].

6.1.1. EFFICIENCY COMPARISON

In this section the efficiencies that are calculated using the swirl decay model with the results from CFD simulations. This comparison is made for strong swirling, using the parameter values of table 6.1 unless mentioned otherwise. Slot calculated efficiencies for $FS = 0.30$ with an oil inlet concentration of $\alpha = 0.25$. Slot incorporates the oil inlet concentration α in the CFD simulations by calculating the density and the dynamic viscosity of the mixture, denoted by ρ_m and μ_m respectively. These values for ρ_m and μ_m are then used as the density and dynamic viscosity of the continuous phase. For an oil inlet fraction α , the density and dynamic viscosity of the mixture are calculated using the following formulas [1].

$$\rho_m = \alpha\rho_o + (1 - \alpha)\rho_w \quad (6.1)$$

$$\mu_m = \mu_w(1 - \alpha)^{-2.5 \frac{\mu_o + 0.4\mu_w}{\mu_o + \mu_w}} \quad (6.2)$$

In these equations ρ and μ are the density and the dynamic viscosity. The subscripts m , w and o denote the mixture, water and oil respectively. The values of the density and dynamic viscosity of water and oil are given in table 6.2.

	μ [Pa.s]	ρ [kg/m ³]
Water	$1.183 \cdot 10^{-3}$	1067.8
Oil	$19.4 \cdot 10^{-3}$	881

Table 6.2: The values of the density and dynamic viscosity of oil and water as used by Slot [1].

Using equations 6.1 and 6.2 and the values given in table 6.2, the density and dynamic viscosity of the continuous phase can be calculated for different inlet concentrations α . The calculated values are given in table 6.3.

α	μ_f [Pa.s]	ρ_f [kg/m ³]
0.15	$1.8 \cdot 10^{-3}$	1040
0.25	$2.4 \cdot 10^{-3}$	1021
0.40	$4.1 \cdot 10^{-3}$	993

Table 6.3: The calculated values of the density and dynamic viscosity of oil-water mixtures for different oil inlet concentrations α .

Using the values of table 6.3 calculations can be done for different values of α . These values are different than the values given in table 6.1, which gives the values of μ_f and ρ_f for $\alpha = 0$. With the calculated values of table 6.3 a good comparison can be made with the CFD simulations and experimental results. Slot has performed efficiency calculations for different particle diameters D_p for oil inlet concentration $\alpha = 0.25$. Table 6.4 shows the efficiencies calculated by Slot [1] using CFD and the efficiencies calculated using the swirl decay model for strong swirling.

D_p [μm]	η_{CFD}	η_{sdm}
50	0.61	0.41
75	0.79	0.65
100	0.86	0.99

Table 6.4: Comparison between the calculated efficiencies of CFD simulations by Slot and the swirl decay model for different particle diameters D_p . The oil inlet fraction is $\alpha = 0.25$ and the calculations are for strong swirling.

In table 6.4 η_{CFD} is the efficiency calculated by Slot using CFD and η_{sdm} is the efficiency calculated using the swirl decay model for the same input parameters. This is illustrated in figure 6.2.

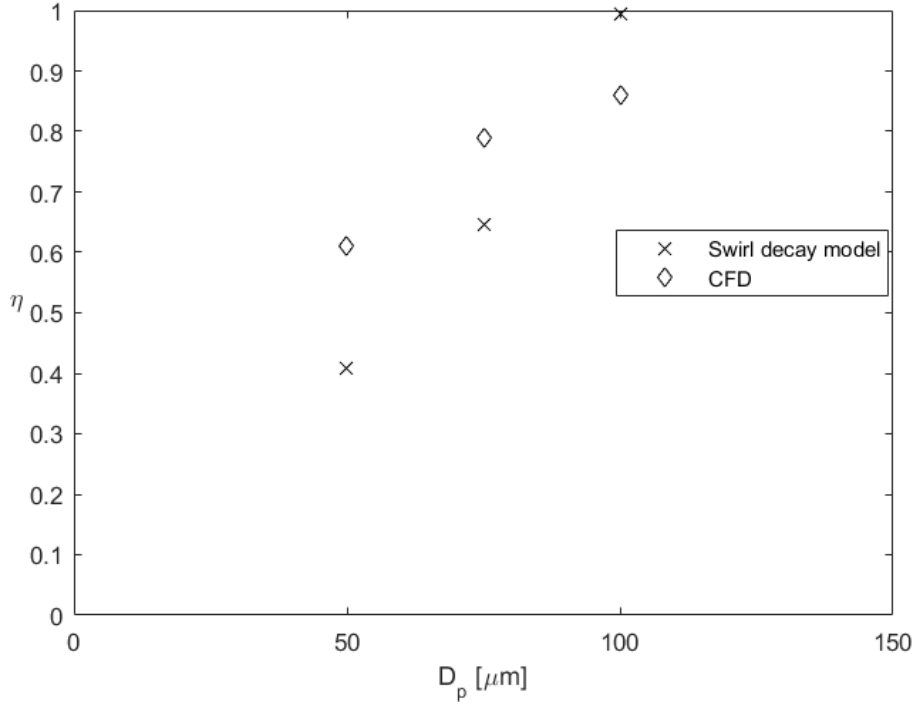


Figure 6.2: Comparison between efficiencies calculated using CFD by Slot and the swirl decay model for different particle diameters D_p and strong swirling. The oil inlet concentration is $\alpha = 0.25$.

The values from table 6.4 and figure 6.2 show that for these specific input values for $D_p = 50\mu\text{m}$ and $D_p = 75\mu\text{m}$ the swirl decay model predicts lower efficiency values than the CFD simulations. However, it can also be seen that between $D_p = 50\mu\text{m}$ and $D_p = 100\mu\text{m}$ the predicted efficiency from the swirl decay model decreases at a much higher rate than the predicted efficiency from the CFD. From this it can be concluded that the swirl decay model is more sensitive to changes in D_p than the CFD simulations. This could have been expected, since the results in section 5.3.1 show that the swirl decay model displays a large sensitivity to D_p for $40\mu\text{m} < D_p < 65\mu\text{m}$ for strong swirling, as illustrated in figure 5.1. For example, the difference in efficiency calculated by the swirl decay model between $D_p = 50\mu\text{m}$ and $D_p = 100\mu\text{m}$ is $\Delta\eta = 0.49$ while for the same D_p range the CFD simulations only predict an increase of $\Delta\eta = 0.25$. This illustrates how sensitive the swirl decay model is for D_p in this particular range and how important it is to use the right value for D_p to find the most accurate prediction.

6.2. COMPARISON WITH EXPERIMENTS

This section compares the results from the swirl decay model to the experimental results from van Campen [2]. As mentioned on multiple occasions throughout this thesis, the particle diameter D_p plays an important role in the separation efficiency of the swirl decay model. Therefore, when comparing the swirl decay model to the experimental results from van Campen, it will be attempted to use values for D_p that are as representative as possible. Since the swirl decay model describes the trajectory of the particle downstream of the swirl element, droplet sizes will be used that van Campen measured downstream of the swirl element. The input parameters that were used by van Campen are listed in table 6.5. ω_s is the vorticity for strong swirling, ω_w is the vorticity for weak swirling. The droplet size distribution as measured by van Campen for strong and weak swirling is shown in figure 6.3.

L	$=$	1.70 m	μ_f	$=$	$1.183 \cdot 10^{-3}$ Pa.s
D_o	$=$	0.1 m	ρ_f	$=$	1067.8 kg/m ³
D_i	$=$	0.05 m	ρ_p	$=$	881 kg/m ³
U_z	$=$	2.0 m/s	ω_s	$=$	502 s ⁻¹
D_v	$=$	0.09 m	ω_w	$=$	360 s ⁻¹

Table 6.5: The standard values for the key parameters that are used for the numerical simulations when comparing the base model to CFD simulations by Slot. Values from Slot [1].

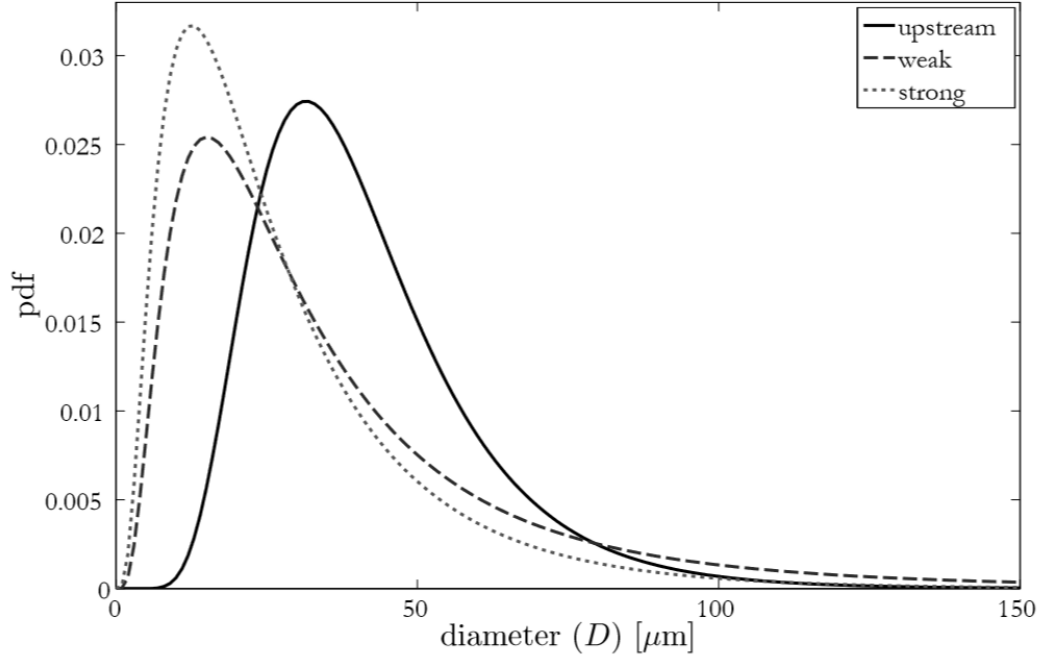


Figure 6.3: PDF of the number of droplets upstream and downstream of the strong and weak swirl element as a function of the droplet size. This distribution is determined experimentally by van Campen. Figure from van Campen [2].

Figure 6.3 shows that the median particle diameter D_p shifts towards the left for both weak and strong swirling with respect to the upstream distribution. In this model the situation downstream of the swirl element is considered, so the droplet size distribution downstream of the strong and weak swirling element will be used. To calculate the efficiency based on this droplet size distribution this continuous distribution is divided into bins of $10\mu\text{m}$ each. Then the relative volumetric contribution of the droplets of different sizes is calculated. With this information it can be calculated what percentage of the total volume is contributed by each droplet size category. Then, using the efficiencies that belong to each droplet size and taking the volumetric weighted sum of these separate efficiencies, the efficiency is calculated. The approximations of the droplet size distribution for strong and weak swirling are shown in Appendix C. Using these approximations it can be determined whether the efficiencies calculated by taking the median D_p are significantly different than the efficiencies calculated by using the droplet size distribution. The results are displayed in table 6.6.

	D_p [μm]	η_1	η_2
strong	18	0.280	0.802
weak	23	0.286	0.821

Table 6.6: Comparison between the efficiency η_1 calculated for the median droplet size and the volumetric weighted efficiency η_2 . D_p in this table is the median droplet diameter. Results for strong and weak swirling.

Table 6.6 shows a comparison between efficiencies calculated in two different ways based on the droplet size distribution of van Campen. η_1 is calculated using the median particle diameter, denoted as D_p in the table. η_2 is the efficiency calculated using the volumetric weighted droplet size distribution. As can be seen,

the median droplet size for strong swirling does not differ much from the weak swirling. When taking these median particle diameters and the input values of table 6.5 efficiency η_1 is found. As can be seen in table 6.6 there is a large difference between η_1 and η_2 . Therefore it can be concluded that it is important to take the droplet size distribution into account when calculating the efficiency. Table 6.6 also shows that it should not be assumed that droplets have the same diameter for weak swirling as for strong swirling. Using the experimental results of the droplet size distribution actually yields a slightly higher efficiency for weak swirling than for strong swirling. This shows the importance of carefully picking the input value of D_p for the swirl decay model.

Now that the volumetric weighted efficiency is calculated based on the droplet size distribution found by van Campen, the result can be compared to the experimental values found by van Campen. Van Campen experimentally determined the separation efficiency for strong swirling and different oil inlet concentrations α . The efficiencies calculated using the swirl decay model for strong swirling, FS=0.25 and different oil inlet concentrations α are given in table 6.7. For these calculations the droplet size distribution for strong swirling is taken into account and the values of table 6.3 and 6.5 are used.

α	η
0.15	0.75
0.25	0.64
0.40	0.42

Table 6.7: The efficiency calculated by the swirl decay model for different oil inlet concentrations α . Calculations done for strong swirling and FS=0.25. The input values that are used can be found in tables 6.3 and 6.5.

The dilute efficiency η_{dilute} is defined similar to the definition for efficiency used in this thesis, so the results will be compared to this efficiency. Figure 6.4 shows a comparison between CFD simulations, experimental values and the swirl decay model. The figure shows efficiency values calculated for different oil inlet concentrations.

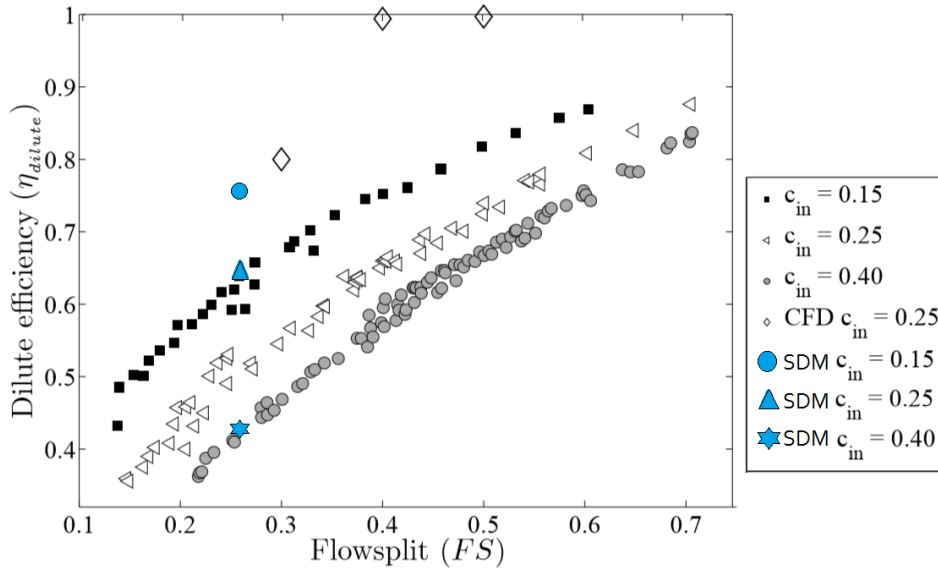


Figure 6.4: Comparison between the dilute efficiency calculated by van Campen, Slot and the swirl decay model for different oil inlet concentrations c_{in} and different values for the flow split. The swirl decay values are labeled by SDM. Calculations for strong swirling. Figure by van Campen [2].

In figure 6.4 the oil inlet concentration, in this thesis referred to as α , is denoted as c_{in} . From figure 6.4 it can be concluded that the CFD simulations as well as the swirl decay model predict higher efficiencies than the values experimentally obtained by van Campen. However, the swirl decay model seems to give a better prediction than the CFD simulations. This is most likely due to the fact that for these calculations the swirl decay model has taken the droplet size distribution into account whereas the CFD simulations have used a

constant droplet size of $D_p = 100\mu\text{m}$. From figure 6.4 it can also be seen that for different values of c_{in} the swirl decay model follows the trend of the experimental results. For increasing c_{in} the swirl decay model predicts smaller values for η , which is confirmed by the experimental results. Generally the predicted efficiencies of the swirl decay model are slightly higher than the experimental values. However, for $c_{in} = 0.40$ the predicted η is close to the experimental value.

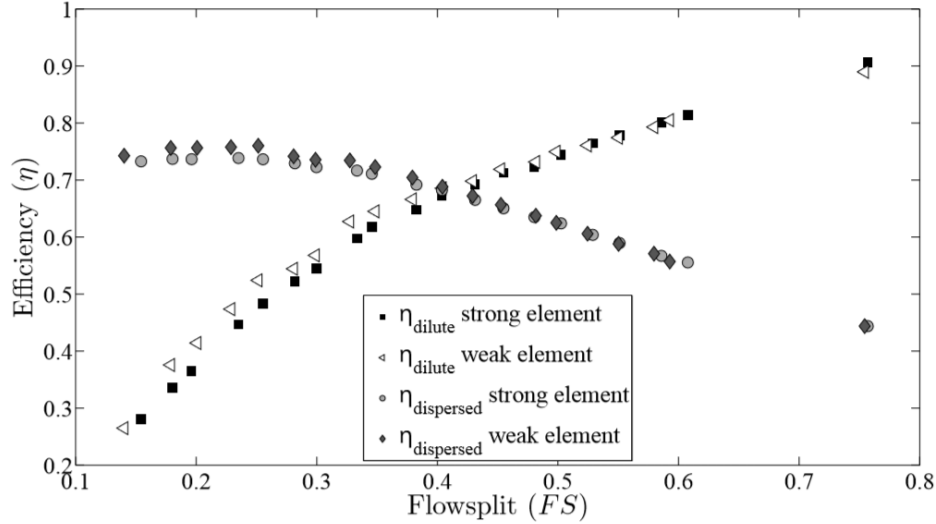


Figure 6.5: The dilute efficiency experimentally determined by van Campen for weak and strong swirl, different FS values and $c_{in} = 0.25$. Figure by van Campen [2].

For weak swirling the best comparable result by van Campen is for $c_{in} = 0.25$ and $FS = 0.25$. This result is shown in figure 6.5. Van Campen found that $\eta = 0.48$ for these conditions, where the swirl decay model predicts $\eta = 0.56$. This is a lower efficiency than the swirl decay model predicts for strong swirling under the same conditions, as opposed to the experimental results, which show a higher efficiency for weak swirling. However, the swirl decay model predicts a reasonable efficiency value for both strong and weak swirling. Furthermore, the inlet concentration of oil c_{in} and the flow split FS seem to have a significant influence on the separation efficiency.

6.3. CONCLUSIONS

Based on the comparison between the swirl decay model and CFD simulations and experimental results the following conclusions can be drawn:

1. The swirl decay model is more sensitive to the particle diameter D_p than the CFD simulations by Slot. This can be concluded from the efficiency comparison for different particle diameters. For more representative values for D_p the efficiency calculated by the swirl decay model is closer to the efficiency calculated by using CFD than for larger values of D_p .
2. Taking the droplet size distribution into account results in significantly different efficiency values for the swirl decay model. This shows that simply taking the median D_p is an over-simplification.
3. The efficiency values calculated with the swirl decay model based on the droplet size distribution found by van Campen [2] are generally larger than the efficiency values that are found experimentally by van Campen.
4. When taking the droplet size distribution and the oil inlet concentration α into account, the swirl decay model predicts reasonable values for the efficiency, although slightly higher than the experimental values. However, the general trends for changing the inlet oil concentration is predicted reasonably well by the swirl decay model.
5. The inlet concentration of oil c_{in} and the flow split FS seem to have a significant influence on the separation efficiency.

7

CONCLUSIONS AND RECOMMENDATIONS

In this chapter conclusions will be drawn and the research question will be answered. As stated in the introduction, the research question of this thesis is

To what extent can a mechanistic model predict the separation performance of an in an in-line liquid-liquid swirl separator?

After the research question has been answered, recommendations will be made for further development of the mechanistic model of an in-line liquid-liquid swirl separator.

7.1. CONCLUSION

In this report a study has been conducted on the modeling of an in-line liquid-liquid swirl separator, which is a method that, if developed accordingly, could be of great value to the oil industry. To model the process of separating an oil-water mixture using an in-line liquid-liquid swirl separator different research steps have been taken. The first step was building a base model. The idea of this model was to provide a solid foundation for a more sophisticated model. This model is described in chapter 3. By analyzing the results that this base model provided and comparing these results to CFD simulations done by Slot [1] and experimental results from van Campen [2], some conclusions could be drawn. Based on these conclusions a more sophisticated model was built, referred to as the swirl decay model in this thesis. The most important conclusions based on the base model were:

1. The particle diameter D_p of the oil droplet has a large influence on the separation efficiency.
2. Swirl decay throughout the swirl tube should not be neglected.
3. A Gaussian vortex profile is a good approximation of the azimuthal velocity profile in an in-line liquid-liquid swirl separator.
4. Like the base model, CFD results from Slot also predict higher efficiency values than the efficiency values experimentally found by van Campen. Therefore a more sophisticated flow field cannot be the main reason for this aberrant result.

Based on these conclusions, an improved model was built which takes swirl decay and the Gaussian vortex profile into account. By analyzing the results that this swirl decay model provided and comparing these results to CFD simulations done by Slot and experimental results from van Campen, some conclusions can be drawn and recommendations for further sophistication of the model can be made. The most important conclusions based on the swirl decay model in addition to conclusions drawn previously were:

5. At some point increasing the length of the swirl tube L does not result in a higher efficiency anymore. This is due to swirl decay. At some point the circulation will become 0 due to this decay, at which point the inward radial velocity of the oil particle will become 0 as well and the efficiency stops increasing. Due to diffusion increasing L beyond a certain point may even decrease the separation efficiency.

6. Realistic swirl decay coefficients of $0.01 < C_{dc} < 0.1$ significantly influence the efficiency of the swirl separator. Therefore C_{dc} should be determined as accurately as possible for the best possible result.
7. The swirl decay model is more sensitive to the particle diameter D_p than the CFD simulations by Slot.
8. For more representative values for D_p the efficiency calculated by the swirl decay model is closer to the efficiency calculated by using CFD than for larger values of D_p . Taking the droplet size distribution into account results in significantly different efficiency values for the swirl decay model. This shows that simply taking the median D_p is an over-simplification.
9. The efficiency values calculated with the swirl decay model based on the droplet size distribution found by van Campen [2] are generally larger than the efficiency values that are found experimentally by van Campen.
10. The experimental results from van Campen show that the inlet concentration of oil c_{in} and the flow split FS seem to have a significant influence on the separation efficiency.
11. The effects of changing the oil inlet concentration c_{in} can be partially captured by calculating the density and dynamic viscosity of the continuous phase based on the oil-water mixture.

The mechanistic model that was built in this research can predict the efficiency values to some extent, although only under specific circumstances. The most sophisticated version of the mechanistic model, referred to as the swirl decay model, generally calculates larger efficiency values than the values that are found experimentally. However, the model generally seems to be able to qualitatively predict the way the efficiency changes when changing parameters, although the exact numerical values differ slightly from the experimental values. To accurately predict the efficiency of an in-line swirl separator some more features should be incorporated in the model. For these improvements recommendations will be made.

7.2. RECOMMENDATIONS

This section addresses the recommendations for further sophistication of the mechanistic model. These recommendations are based on the findings of this report.

1. The swirl decay coefficient C_{decay} is assumed to have a constant value in this research. However, according to Dirkzwager [7], the swirl decay coefficient is not constant and generally increases for larger swirl numbers. Since the swirl decay coefficient can have a large influence on the separation efficiency as shown in section 5.3 it will be highly beneficial for the accuracy of the model to determine the swirl decay coefficient accurately.
2. The experimental results of van Campen show that the oil inlet concentration has a large influence on the efficiency value. This is partly due to droplet breakup and coalescence effects. Since droplet coalescence and breakup changes the particle diameter D_p , these effects are significant to implement in a more sophisticated model.
3. Section 6.2 illustrates the significance of the distribution of the droplet particle size on the separation efficiency. It would be beneficial for the model to model the distribution of the particle size. This is directly correlated to the coalescence and breakup effects mentioned in the previous recommendation.
4. The experimental results from van Campen show that the flow split FS significantly influences the separation efficiency. This is something that would be relatively uncomplicated to add to the model, by using a block-shaped axial velocity profile.
5. The CFD simulations by Slot show that the diameter of the vortex D_v decreases downstream due to vortex breakdown. However, both the base model and swirl decay model assume D_v to be constant. For a more realistic model this decay of D_v should be taken into account.

A

ADDITIONAL BASE MODEL RESULTS

In this appendix additional results of the base model can be found. These results include results from the non-dimensional analysis described in section 3.4 and results from the influence of separate parameters on the separation efficiency as described in section 3.6.

A.1. NON-DIMENSIONAL RESULTS

In this section the influence of different non-dimensional numbers on the separation performance are discussed as described in section 3.4. When keeping all other non-dimensional number constant, varying some non-dimensional numbers does not influence the efficiency, as can be seen in figure A.4.

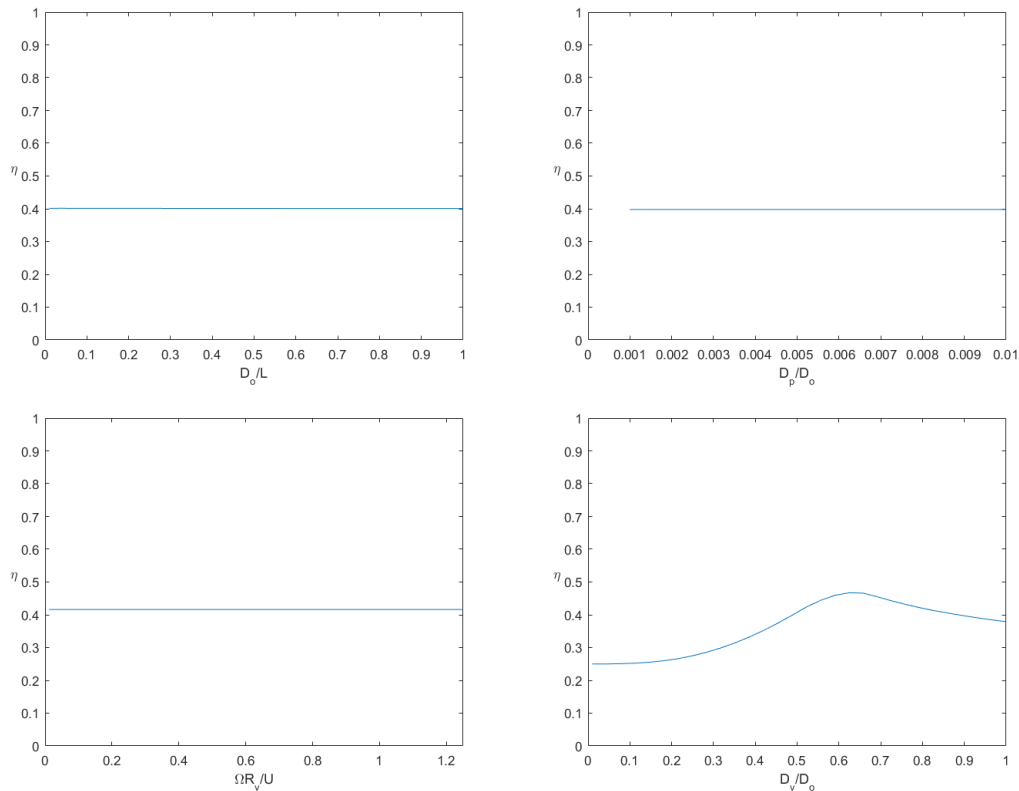


Figure A.1: The influence of changing non-dimensional numbers on the separation efficiency while keeping other non-dimensional numbers constant. The influence of the parameters is displayed as follows. Top left: $\frac{D_o}{L}$, Top right: $\frac{D_p}{D_o}$, Bottom left: $\frac{\Omega R_v}{U}$, Bottom right: $\frac{D_v}{D_o}$. As can be seen from the figure, none of these non-dimensional numbers influences the efficiency when the other non-dimensional numbers are kept constant.

As can be seen in figure A.4, varying $\frac{D_o}{L}$, $\frac{D_p}{D_o}$ and $\frac{\Omega R_v}{U_z}$ while keeping all other non-dimensional numbers constant at the values given in table 3.1 does not have any effect on the separation efficiency η . This is because the effects of these non-dimensional numbers are already compensated by keeping the other non-dimensional numbers constant. It can be seen in figure A.4 that the efficiency does show an increase for certain values of $\frac{D_v}{D_o}$. However, at some point the efficiency starts to decrease again. When considering that all other non-dimensional numbers are kept constant, this result makes sense. When increasing D_v and therefore $\frac{D_v}{D_o}$, ω must be decreased in order to keep $\frac{\Omega R_v}{U_z}$ constant for a constant U_z . Therefore at some point increasing $\frac{D_v}{D_o}$ does not result in a higher efficiency anymore, as ω becomes smaller and the efficiency decreases again. The value of $\frac{D_v}{D_o}$ for which the efficiency start going down again depends on the chosen values for $\frac{F_B}{F_I}$ and $\frac{\Omega R_v}{U_z}$ but based on just the value of $\frac{D_v}{D_o}$ it can never be concluded that a certain change in efficiency occurs for changing $\frac{D_v}{D_o}$. Therefore changing the value of $\frac{D_v}{D_o}$ alone does not influence the separation efficiency.

One non-dimensional number that does influence the separation efficiency is $\left(\frac{D_i}{D_o}\right)^2$. However, this dependency is predictable and therefore it was not presented in the main text. This dependency is displayed in the figure below.

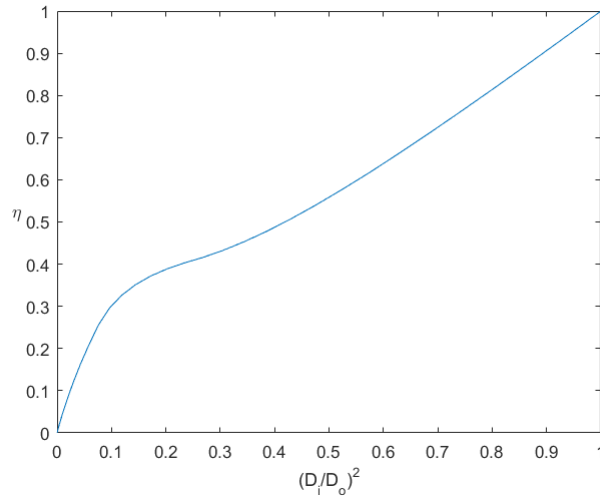


Figure A.2: The influence of $\left(\frac{D_i}{D_o}\right)^2$ on the separation efficiency η .

As expected the efficiency depends roughly linearly on $\left(\frac{D_i}{D_o}\right)^2$. The only aberration from a linear dependency is the lump that can be seen around $\left(\frac{D_i}{D_o}\right)^2 = 0.2$. This lump is caused by the choice of $\frac{D_v}{D_o} = 0.5$. This is due to the characteristics of a Rankine vortex, which is used in the base model. For a Rankine vortex the azimuthal velocity increases linearly for $r < R_v$ and then decreases again. Therefore the efficiency increases quickly at the beginning of the curve and then starts growing towards linear dependency again. When a larger value for $\frac{D_v}{D_o}$ would be used, this lump would be shifted to the right and for smaller values the lump would be shifted to the left. This near-linear dependency makes sense when all other non-dimensional numbers are kept constant, as $\left(\frac{D_i}{D_o}\right)^2$ only influences the area of the pickup tube in this model.

A.2. PARAMETER RESULTS

This section presents results obtained by varying the key parameters of the base model individually. The diameter of the pickup tube D_i determines the maximum radial position of the particle at the end of the swirl tube at which the particle is collected. An increase in D_i means that a larger fraction of the particles will be accepted as collected and therefore an increase in η . The separation efficiency as a function of $(D_i/D_o)^2$ is shown in figure A.3. For these calculations the parameters of table 3.2 are used, except that $\omega = 150$ and D_i has been varied.

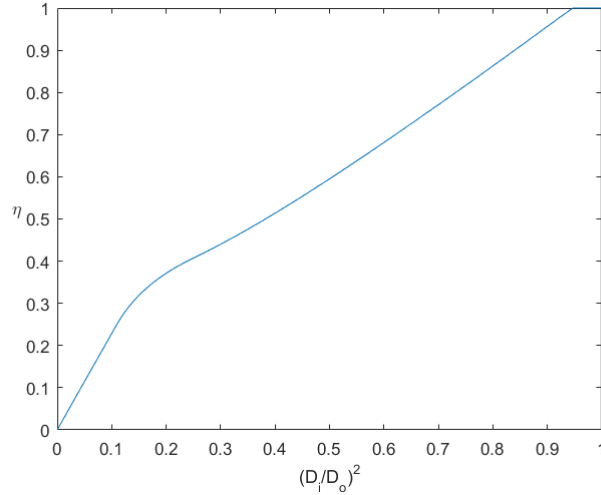


Figure A.3: The influence of D_i/D_o on the separation efficiency η of the base model.

Figure A.3 shows a near-linear increase in η for increasing $(D_i/D_o)^2$. This is expected as can be understood from equation 3.13. However, the relation is not completely linear. A lump can be seen around $(D_i/D_o)^2 = 0.2$. This can be explained by realizing that $D_v/D_o = 0.5$ and because of that the efficiency is expected to increase slightly faster than linearly to the point where the radial start position exceeds the vortex radius. Also, the efficiency already reaches the value of 1 at $(D_i/D_o)^2 = 0.94$. This is because of the radial displacement of the particle in the swirl tube. Therefore a particle starting at $r = R_o$ will end up at $r < R_o$ at the end of the pipe. As expected $\eta = 0$ for $D_i/D_o = 0$ as no particles can be collected in a tube with a diameter of 0. The results of varying 4 other parameters are shown below.

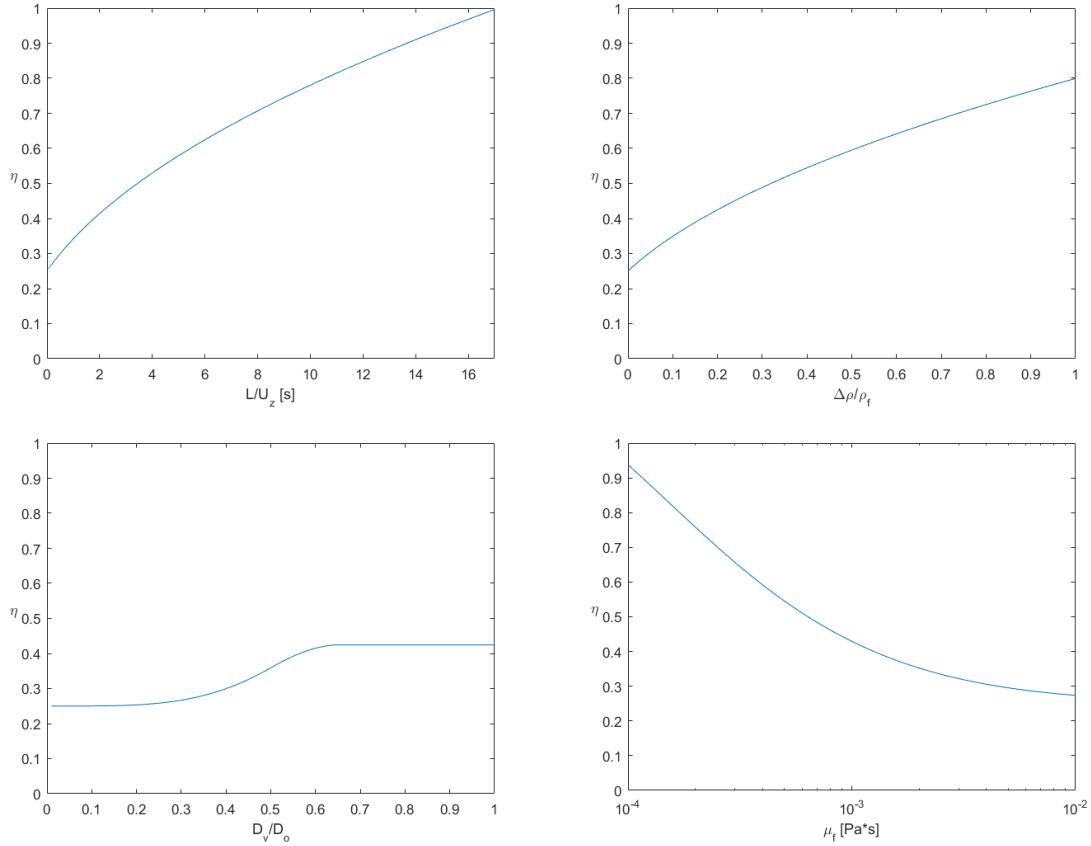


Figure A.4: The influence of changing parameters on the separation efficiency while keeping other parameters constant. The influence of the parameters is displayed as follows. Top left: $\frac{L}{U_z}$, Top right: $\frac{\Delta\rho}{\rho_f}$, Bottom left: $\frac{D_v}{D_o}$, Bottom right: μ_f .

These results are as could be expected. For increasing $\frac{L}{U_z}$, the particle has a relatively long traveling time in the swirl tube, giving it a longer time to travel radially inwards, resulting in a higher efficiency. It can also be seen that for $L = 0$, the efficiency is $\eta = 0.25$. This makes sense, because for this model a constant flow split of $FS = 0.25$ is assumed (eq. 2.15). For increasing $\frac{\Delta\rho}{\rho_f}$ the efficiency increases as well. This makes sense as the buoyancy force increases with $\Delta\rho$ according to equation 2.18. Once again an efficiency of $\eta = 0.25$ is observed for $\frac{\Delta\rho}{\rho_f} = 0$ as expected. The efficiency generally increases for increasing $\frac{D_v}{D_o}$, which makes sense as this ratio determines the radius of the forced region of the Rankine vortex, where azimuthal velocities are large. Again, $\eta = 0.25$ is observed for $\frac{D_v}{D_o} = 0$, which makes sense since for that case there is no forced vortex and no azimuthal velocity. For increasing μ_f the efficiency decreases. This can be explained, because a fluid with higher viscosity results in a larger resistance when the particle moves relative to the fluid. Therefore it will be more difficult for the partial to travel radially inwards, resulting in a lower efficiency. It can be seen that for high μ_f the familiar efficiency of $\eta = 0.25$ is approached. This makes sense, because a fluid with infinitely large viscosity is very difficult to travel through, and therefore the radial position of the particle will hardly differ at the end of the swirl tube compared to the beginning of the tube.

B

ADDITIONAL SWIRL DECAY MODEL RESULTS

In this appendix additional results of the swirl decay model can be found which is described in chapter 5. These results include the influence of separate parameters on the separation efficiency as described in section 5.3.

B.1. PARAMETER RESULTS FOR STRONG SWIRLING

This section presents results obtained by varying the key parameters of the base model individually for strong swirling. The input parameters that are used can be found in table 5.1 unless mentioned otherwise.

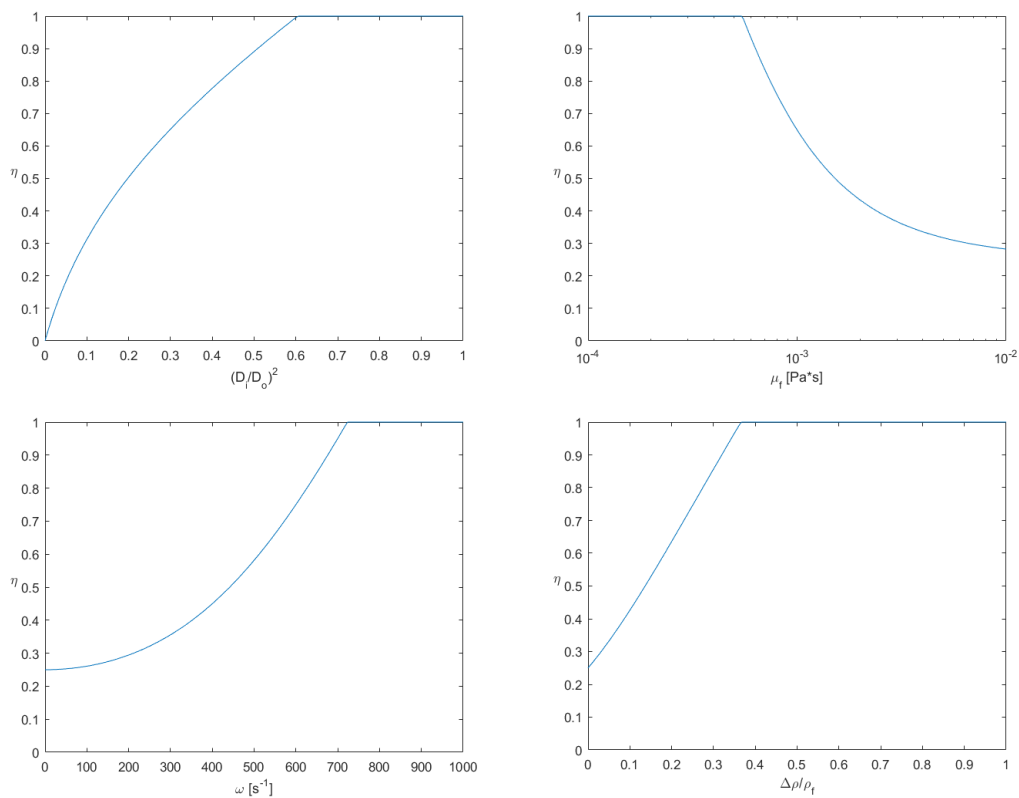


Figure B.1: The influence of changing key parameters individually on the separation efficiency η while keeping other key parameters constant. The influence of the parameters is displayed as follows. Top left: $(\frac{D_i}{D_o})^2$, Top right: μ_f , Bottom left: ω , Bottom right: $\frac{\Delta\rho}{\rho_f}$. The results are for strong swirling.

C

EXPERIMENTAL DROPLET SIZE DISTRIBUTION APPROXIMATION

This appendix shows the approximations that were used to calculate the efficiency in section 6.2 based on the droplet size distribution as found by van Campen [2]. To approximate the droplet size distributions, the droplets have been sorted into bins of $10\mu\text{m}$ each. By taking the middle of the bin as the value of D_p representing that bin and by taking the pdf value of the curve at the middle of the bin, the approximations are done as shown in figure C.1

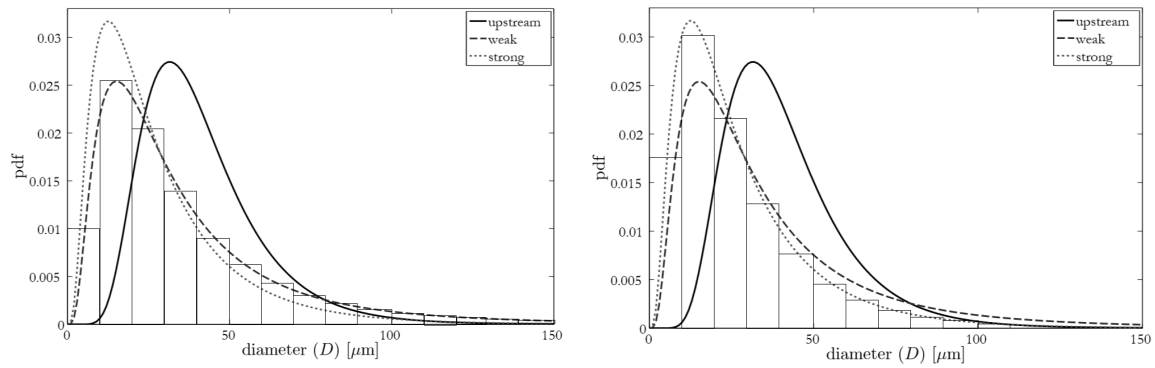


Figure C.1: The bar chart approximating the particle size distributions of weak and strong swirling. Experimental results by van Campen [2]. On the left the approximation for weak swirling. On the right the approximation for strong swirling.

Using that each bin has a width of $10\mu\text{m}$ the following values are found for strong and weak swirling.

D_p [μm]	5	15	25	35	45	55	65	75	85	95	105	115	125	135	145
p_{weak}	0.10	0.25	0.20	0.13	0.09	0.07	0.04	0.03	0.02	0.02	0.01	0.01	0.01	0.01	0.01
p_{strong}	0.18	0.30	0.22	0.13	0.08	0.05	0.03	0.02	0.02	0.01	0.01	0	0	0	0

Table C.1: The probabilities of finding a particle in the bin with bincenter D_p for weak and strong swirling.

Using these values from table C.1 and by calculating the volume of a particle for all values of D_p , the volume fraction that each bar contributes to the total volume can be calculated. Then, using the efficiency for a particle of each value for D_p and multiplying these efficiency values by its volumetric weight, the total efficiency can be calculated by taking the sum of these volumetric weighted contributions. The efficiency values that are used for this are listed in tables C.2, C.3, C.4 and C.5. The first two tables show efficiencies for strong and weak swirling and oil inlet concentration $\alpha = 0$ and $\alpha = 0.25$ respectively. Tables C.4 and C.5 give efficiency values for $\alpha = 0.15$ and $\alpha = 0.40$ respectively.

D_p [μm]	5	15	25	35	45	55	65	75	85	95	105	115	125	135	145
η_{weak}	0.25	0.26	0.29	0.32	0.37	0.45	0.53	0.64	0.76	0.90	1	1	1	1	1
η_{strong}	0.25	0.27	0.32	0.40	0.51	0.66	0.85	1	1	1	1	1	1	1	1

Table C.2: The efficiencies of particles with particle diameter D_p for strong and weak swirling for $\alpha = 0$.

D_p [μm]	5	15	25	35	45	55	65	75	85	95	105	115	125	135	145
η_{weak}	0.25	0.25	0.26	0.28	0.30	0.32	0.35	0.38	0.42	0.47	0.53	0.59	0.66	0.74	0.82
η_{strong}	0.25	0.26	0.29	0.32	0.38	0.45	0.54	0.65	0.78	0.92	1	1	1	1	1

Table C.3: The efficiencies of particles with particle diameter D_p for strong and weak swirling for $\alpha = 0.25$.

D_p [μm]	5	15	25	35	45	55	65	75	85	95	105	115	125	135	145
η_{strong}	0.25	0.27	0.31	0.37	0.45	0.57	0.71	0.88	1	1	1	1	1	1	1

Table C.4: The efficiencies of particles with particle diameter D_p for strong swirling for $\alpha = 0.15$.

D_p [μm]	5	15	25	35	45	55	65	75	85	95	105	115	125	135	145
η_{strong}	0.25	0.26	0.27	0.28	0.30	0.33	0.37	0.42	0.47	0.54	0.61	0.69	0.78	0.88	0.98

Table C.5: The efficiencies of particles with particle diameter D_p for strong swirling for $\alpha = 0.40$.

The resulting efficiencies are presented in section 6.2.

BIBLIOGRAPHY

- [1] J. J. Slot, *Development of a centrifugal in-line separator for oil-waterflows*, PhD Thesis, University of Twente (2013).
- [2] L. van Campen, *Bulk Dynamics of Droplets in Liquid-Liquid Axial Cyclones*, PhD thesis, Delft University of Technology (2014).
- [3] O. Kristiansen, *Compact, inline separation technology - what and why?* Norwegian University of Science and Technology guest lecture, Trondheim (2012).
- [4] H. Bjartnes, R. Westra, B. Knudsen, and B. Ibouhouten, *Qualification of inline dewatering technology*, Society of Petroleum Engineers, Aberdeen (2013).
- [5] A. Ashok, *Development of an oil-water separator report for Rijksdienst voor Ondernemend Nederland*, Tech. Report, Delft University of Technology (2017).
- [6] S. K. Star, *Pressure distribution in a liquid-liquid cyclone separator*, MSc thesis, Delft University of Technology (2016).
- [7] M. Dirkwager, *A new axial cyclone design for fluid-fluid separation*, PhD thesis, Delft University of Technology (1996).
- [8] R. Knöbel, *Experimental study on the separation of oil and water using and axial in-line cyclone*, MSc thesis, Delft University of Technology (2017).
- [9] W. Steenbergen, *Turbulent pipe flow with swirl*, PhD thesis, Eindhoven University of Technology (1995).
- [10] S. Schütz, G. Gorbach, and M. Piesche, *Modeling fluid behavior and droplet interactions during liquid-liquid separation in hydrocyclones*, Vol. 64 (Chemical Engineering Science, 2009) pp. 3935–3952.
- [11] C. Crowe, J. Schwarzkopf, M. Sommerfeld, and Y. Tsuji, *Multiphase flows with droplets and particles*, CRC Press, Boca Raton (2012).
- [12] G. Hauke, *An Introduction to Fluid Mechanics and Transport Phenomena*, Springer, Zaragoza (2008).

